Chemical Engineering Science 202 (2019) 250–269

Contents lists available at ScienceDirect

Chemical Engineering Science

journal homepage: www.elsevier.com/locate/ces

Explosively driven hierarchical particle jetting

Kun Xue [a,*], Jiaqi Liu [a], Chun Feng [b], Yixiang Gan [c], Chunhua Bai [a]

[a] State Key Laboratory of Explosive Science and Technology, Beijing Institute of Technology, Beijing 100081, China
[b] Key Laboratory for Mechanics in Fluid Solid Coupling Systems, Institute of Mechanics, Chinese Academy of Sciences, Beijing 100190, China
[c] School of Civil Engineering, The University of Sydney, Sydney, Australia

HIGHLIGHTS

- Explosive driven particle jetting is modeled by a FEM-DEM coupling method.
- The origin of a distinctive hierarchical particle jetting pattern is identified.
- The meso-scale mechanisms underlying the jetting pattern are revealed.
- Microstructure of particle packings significantly affects the jetting patterns.

GRAPHICAL ABSTRACT

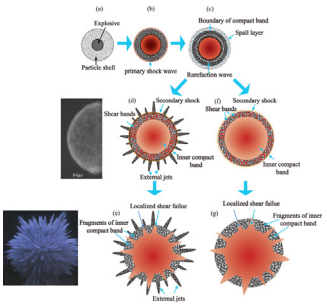

ARTICLE INFO

Article history:
Received 22 October 2018
Received in revised form 8 March 2019
Accepted 17 March 2019
Available online 19 March 2019

Keywords:
Hierarchical particle jetting
Explosive dispersal
Coupled DEM and FEM
Shear bands
Particle packing structure

ABSTRACT

When particle rings/shells are subjected to divergent explosive loadings, a dual overlapping particle jetting structure emerges during the shock interaction timescale which consists of a large number of minor jets initiated from the external interface at very early instants and a much reduced number of major jets formed from the internal interface at delayed times but overtaking the minor jets in later times. In the present work, the formation of the hierarchical particle jetting pattern is investigated numerically by discrete element method (DEM) coupled with finite element method (FEM), which execute the mechanical calculations of particles and the explosive/detonation gases, respectively. The numerical results find that the external jetting arises from the spallation of an outer layer pulled away by inward propagating rarefaction waves. Meanwhile an inner compact band re-compressed by a secondary shock remains densely packed while expanding outward. The fragmentation of the inner compact particle band, preceding the internal particle jetting, is caused by the profuse spiral shear failures expanding from the inner radius to the outer radius. The resultant jetting structure depends on the shear-band spacing and the grouping of the clockwise and counterclockwise shear bands as well. The former is a function of the bulk characteristics of the inner compact band, especially the resistance to the shear flows. The latter markedly varies with the microstructure of particle packing, especially the structural order. In the highly ordered extreme, the particle ring with global crystalline structure exhibits six groups of shear bands, probably giving rise to around six fragments. By contrast, the grouping of shear bands in the amorphous packing is far from definite, suggesting an increased number of much smaller fragments to be generated. The dual jetting structure would degenerate into a single jetting pattern if the inner compact band manages to entrain all the spall particles before the shear failure occurs.

© 2019 Elsevier Ltd. All rights reserved.

* Corresponding author.
E-mail address: xuekun@bit.edu.cn (K. Xue).

https://doi.org/10.1016/j.ces.2019.03.043
0009-2509/© 2019 Elsevier Ltd. All rights reserved.

1. Introduction

Particle jetting during the explosive or shock dispersal of particles has been widely observed in nature and many military applications, such as volcanic eruption (Kieffer, 1981), explosion of landmines (Rigby et al., 2018), thermobaric explosion (Ritzel et al., 2009; Bai et al., 2018), high-speed intruder striking granular media, and particle jets impacting targets (Shi et al., 2017; Huang et al., 2010), etc. A typical configuration involves particle rings or shells dispersed by the explosion of central charges (Milne et al., 2010; Ripley et al., 2011;David et al., 2012; Xue et al., 2013; Milne et al., 2014; Ripley and Zhang, 2014; Frost et al., 2017a, 2017b; Bai et al., 2018; Loiseau et al., 2018; Pontalier et al., 2018; Marr et al., 2018). The resultant expanding cloud of disseminated materials comprises of large particle agglomerates which rapidly protrude to finger- or spike-like particle jets as shown in Fig. 1. The formation of explosively driven particle jetting is a subject of fundamental and applied research interests to better understand shock interaction with particles and collective response of particles in extreme conditions as well as engineering applications such as tuning the jetting structure for the purpose of shock mitigation (Pontalier et al., 2018; Rigby et al., 2018), enhancing the jet energy or rendering particle clouds with uniform concentration (Ripley et al., 2011; Xue et al., 2013).

Extensive studies, the bulk of which are field tests using cylindrical or spherical geometries, agree on some fundamental features of the particle jetting phenomenon (Milne et al., 2010; Ripley et al., 2011; Milne et al., 2014; Frost et al., 2017a; Loiseau et al., 2018). Specifically, the particle jetting becomes recognizable during the shock interaction timescale and occurs in the absence of inner and outer casings (Milne et al., 2010; Ripley et al., 2011; Milne et al., 2014; Frost et al., 2017a; Loiseau et al., 2018). Nevertheless there still lacks definite and quantitative characterization of the spatiotemporal evolution of jetting structure largely owning to the difficulties and uncertainties of reconstructing three-dimensional jetting structures from two-dimensional images. Besides, the most determinant factors driving the jetting are still far from clear. Actually the interdependences of many parameters makes it quite challenging to even distinguish the influence of one factor from the other, such as the coupling between the powder fill-to-burster charge mass ratio (F/B) and the geometrical size of particle shell/ring, the correlation between packing density and particle size as well as particle morphology, etc. Thus some dimensionless complex variables rather than the actual structural parameters should be considered as potential driving factors for particle jetting. Frost et al. (2011) first attempted to establish the correlation between the number of jets and a particle compaction Reynolds number which incorporates the effects of density, velocity and effective compaction viscosity of particle shells/rings. But more systematic parametric investigations are needed to corroborate this correlation. In this regard, numerical investigations as performed in this work have special advantages over the experimental means.

Mainly due to the limits aforementioned, there are no widely accepted mechanisms governing the jetting formation and dictating the resulted jetting structure (Milne et al., 2010; Grégoire et al., 2011; Ripley et al., 2011; Xu et al., 2013, 2014; Ripley and Zhang, 2014; Frost, 2018; Loiseau et al., 2018; Osnes et al., 2018). The Rayleigh-Taylor instability (and other hydrodynamic instabilities such as Richtmyer-Meshkov or Kelvin-Helmholz) has been excluded as a possible candidate owing to the inconsistence between the theoretically predicted characteristic timescale and that derived experimentally (Milne et al., 2010; Milne et al., 2014; Ripley and Zhang, 2014). Loiseau et al. (2018) and Frost et al. (2017b) conjectured a brittle fracture model which is based on the assumption that the explosive shock compaction of particles is so strong that intense particle bonding (sintering) enables the particles achieve near solid density. Although this argument is seemly supported by the aluminum fragments collected after the explosive dispersal of aluminum powder layer (Frost et al., 2017a), it is quite contentious to apply this model to the particles with high melting temperatures during quite short shock passage duration. Bearing in mind the particle jetting is universally observed across a wide range of particles, including ceramic grains, soft or hard metallic particles, with or without interstitial fluids (Milne et al., 2010; David et al., 2012; Xue et al., 2013; Milne et al., 2014; Loiseau et al., 2018; Pontalier et al., 2018).

Another aspect which hasn't been taken into account in the previous studies is the microstructure of particle packing. As opposed to solids and fluids, the intrinsic anisotropic packing structure (contact-fabric) of granular materials dictates the corresponding stress structure (force-fabric) which governs the deformation behavior of granular materials (Oda, 1982; Oda et al., 1985; Fu and Dafalias, 2011; Yang et al., 2016). It has been well established that there exists a strong correlation between contact- and force-fabric for granular materials under biaxial and triaxial compression tests (Oda, 1982; Oda et al., 1985; Fu and Dafalias, 2011; Yang et al., 2016). The contact-fabric and the average coordination, as

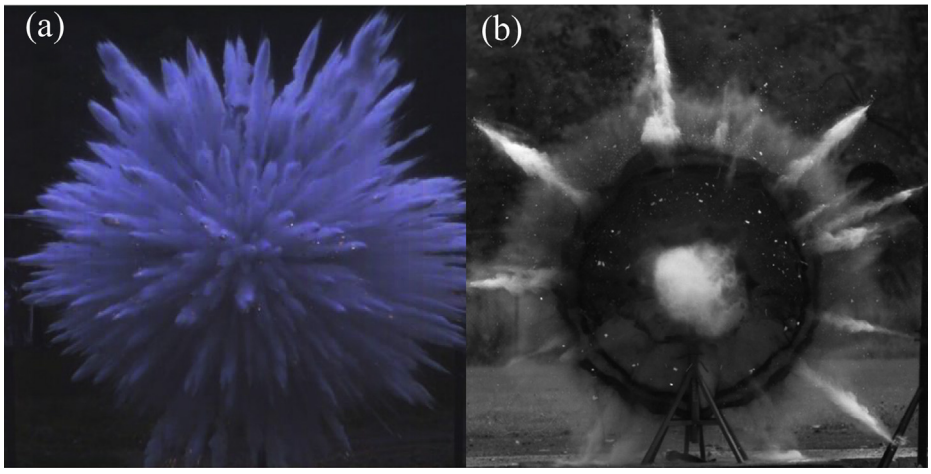

Fig. 1. High-speed photos of explosive dispersal of quartz sand in a spherical geometry (a) and glass beads in a cylindrical geometry (b) taken from Fig. 2 of David et al. (2012) with permission.

the essential microstructural descriptors, have been incorporated into the lately developed constitutive models for the rate-independent rheology of dense granular materials (Sun and Sundaresan, 2011; Vidyapati and Subramaniam, 2016). Sun and Sundaresan (2011) link the closures of the pressure and the friction coefficient to the contact-fabric and the average coordination, whose closures are provided by Vidyapati and Subramaniam (2016). Yet the relationship between the shock propagation and contact-fabric in granular materials has not been fully proposed, let along the influence of fabric on the jetting structure. In the present work, we attempt to explore the role played by the packing structure on the macro-scale jetting structure.

The ultimate goal of this work is to reveal the underlying mechanism of particle jetting which ought to be based on the thorough understanding of the interactions between multiple waves and particles as indicated by many experimental observations. Again, experimental means prove to be inadequate. Numerical method based on continuum theory for granular flows doesn't account for the heterogeneities intrinsic to the particle packings so that *ab initio* perturbations should be imposed artificially (Ripley et al., 2011; Ripley and Zhang, 2014; Ouellet et al., 2017; Osnes et al., 2018). Direct simulation of dense particulate flow under explosive dispersal is capable of accurately resolving coupled shock-shock, shock-particle, and particle-particle interactions (Xu et al., 2013; Mo et al., 2018b). Nevertheless this method can only deal with systems containing relatively small number of particles so that collective flows of massive particles can hardly be taken into account. In the present work, we instead adopt a numerical framework (CDEM®) which incorporates both finite element model (FEM) and discrete element model (DEM) (Feng et al., 2014). The detonation of central explosive and the expansion of detonation gases are modelled by FEM, while particles are modelled by DEM. The detonation pressure calculated by the FEM solver exerted on the particles in contact with the explosive domains through contacts at the interfaces/boundaries. This coupled FEM/DEM approach provides a straightforward and inexpensive means to investigate the relationship between the grain-scale flows and the macroscopic response of granular materials subjected to the detonation.

This paper investigates the hierarchical particle jetting of two-dimensional particle rings driven by central explosion via the coupled FEM/DEM approach. In what follows, we will first present the theory and the implementation of FEM/DEM approach in Section 2. Section 3 gives a detailed account with regard to the preparation of particle rings and the microstructural characterization. The tested cases and simulation procedures are given in Section 4. Section 5 elaborates the simulated explosive dispersal of particles, revealing the key events leading to the hierarchical jetting pattern and the transition of the jetting mode. In Section 6 we compare the proposed jetting mechanism against the rival models based on the experimental observations. Finally a summary of the major findings is given in Section 7.

2. Numerical methodology

The FEM model is used to simulate the detonation of the explosive solids and the expansion of the detonation gases confined inside the particle ring. The DEM is employed to model the particle dynamics driven by the expansion of the detonation gases. Details of the formulations of the FEM and DEM models are presented in Appendices A and B, respectively. The interaction between the explosive FEM elements and particles in contact needs to communicate information between FEM and DEM solvers, i.e. passing the 'deformed mesh' of FEM into DEM as a boundary for particles, and exerting the DEM results of 'wall forces' on the finite elements in return (Zheng et al., 2017). Upon knowing the nodal forces, the nodal displacements of FEM mesh at the new time step can be calculated with FEM. In this way, a real-time and two-way coupling of FEM and DEM can be realized. Details of the coupling algorithm is presented in Appendix C.

The calibration and validation of the proposed FEM-DEM coupled framework (CDEM®) can be found in the previous publications (Yongbo et al., 2016; Feng et al., 2014; Yuan and Shen, 2017). CDEM® has been successfully applied in a variety of fields, especially geotechnical and mining engineering involving explosive loadings (Feng et al., 2014; Yongbo et al., 2016; Yuan and Shen, 2017; Wang et al., 2013).

The coupling FEM and DEM methodology doesn't take into account of the gas effects except the momentum transfer from the detonation gases and the particles in contact. But we argue that the hydrodynamic forces, such as drag force, buoyant force and viscous force, are insignificant in the blast interaction with particles. Experimental and mesoscale numerical studies of the shock compaction of particles found that upon a threshold pressure, normally in the order of $O(10^0)$ GPa, all porosity is removed and the bulk density is near the fully consolidated materials (Vogler et al., 2007; Borg et al., 2009). Secondly the gas infiltration governed by the Darcy's law occurs at much longer time scale than the shock interaction. The interaction between particles and the surrounding flows is minimal compared with the momentum transmission through the contacts and collision between particles sustained by the expansion of the central detonation gases.

3. Microstructure of particle packing

3.1. Generation of particle packings with different particle size distributions

Prior studies have confirmed that random close packings of spherical particles can have a wide range of microstructures in terms of compositional order, bond orientational order, contact fabric, etc. (Schreck et al., 2011; Desmond and Weeks, 2014; Hanifpour et al., 2015; Vidyapati and Subramaniam, 2016; Sun and Sundaresan, 2011). Hence the particle shells used in the experiments which reportedly have the same packing fraction may well have distinct microstructures, probably yielding discernibly varied jetting structures.

For that matter, we numerically generate two different two-dimensional particle packings consisting of circular beads which exhibit distinct microstructural orders as detailed in Section 3.2. These two particle packings have the same average particle diameter (d_0), nearly the same packing fraction (ϕ) and polydispersity (δ), but different particle size distribution in terms of the distribution in diameters, $P(d_p)$. The first distribution is a Gaussian of the form $P(d_p) = A_G \exp\left[-(d_p - d_0)^2/2\sigma^2\right]$, where d_0 is the mean particle diameter, σ is the standard deviation and $A_G = 1/\sqrt{2\pi\sigma^2}$. The other is the uniform distribution with the form of $P(d_p) = 1/2a,\ \ d_p \in [d_0 - a, d_0 + a]$, where d_0 is the mean particle diameter and a defines the lower and upper limits of the range of d_p. The value of a is chosen in a way such that the polydispersity values of packings with either Gaussian or uniform size distributions are identical. The polydispersity is defined as

$$\delta = \sqrt{\left\langle \Delta d_p^2 \right\rangle} / \langle d_p \rangle \tag{1}$$

Here, $\Delta d_p = d_p - \langle d_p \rangle$ and $\langle d_p^2 \rangle = \int (d_p - \langle d_p \rangle)^2 P(d_p) d(d_p)$. For a Gaussian distribution, $\delta = \sigma$. Thus a is set as $a = \sqrt{3} d_0 \sigma$ so that $\delta = \sigma$ for the packing with a uniform distribution. It is the shape rather than the spread of the distribution $P(d_p)$ that distinguishes

one packing from the other. Henceforth the packing with a Gaussian or uniform distribution specified as above is referred to the Gaussian or uniform packing, respectively.

The principles of the numerical protocol for packing generation are to generate a packing with ϕ close to that of a random close packing and maintain the size distribution of the final configuration as close to the predefined distribution as possible. Our method for generating these packings was previously developed in Xu et al. (2005). Briefly, infinitesimal particles are placed randomly in an annular region, gradually expanded, and moved at each step to prevent particles from overlapping. At the beginning of the simulation, particles are assigned radii with a specific distribution and as the particles expand they do so by a multiplicative factor such that the shape of the radii distribution is fixed. To better conform to the circular inner and outer boundaries, the particles placed along the inner and outer perimeters are much smaller than the interior counterparts and all tangential to the inner and outer boundaries. Fig. 2 shows the actual probability density and cumulative density distributions of d_p, $P(d_p)$ and $\Pi(d_p)$, respectively, derived from the particle packings generated via this protocol. The Gaussian (Fig. 2 (a)) and uniform (Fig. 2(b)) packings have identical mean particle diameter, $d_0 = 95.6\ \mu m$, similar polydispersity, $\delta_G = 0.113$, $\delta_U = 0.177$, and packing fraction close to that of the random close packing, $\phi_G = 0.846$ and $\phi_U = 0.832$, respectively.

3.2. Bond orientational order

To quantify structural order which is a key characteristic of the microstructure of particle packing, we calculate the bond orientational order parameter φ_6, which measures the hexagonal registry of nearest neighbors (Hanifpour et al., 2015; Schreck et al., 2011). φ_6 can be calculated "locally", which does not consider phase information, or "globally", which allows phase cancellation. Local and global bond-orientational order parameters in 2D, φ_6^{local} and φ_6^{global} are expressed as

$$\varphi_6^{local}(k) = \frac{1}{n_k}\left|\sum_{j=1}^{n_k} e^{6i\theta_{kj}}\right|, \tag{2}$$

$$\varphi_6^{global} = \frac{1}{N}\left|\sum_{k=1}^{N}\frac{1}{n_k}\sum_{j=1}^{n_k} e^{6i\theta_{kj}}\right|, \tag{3}$$

where θ_{kj} is the angle between a central particle k and neighbor j, and n_k denotes the number of nearest neighbors of k. Using φ_6^{local} we can readily identify and characterize the locally motifs within the packing. For 2D packing, $\varphi_6^{local} = 1$ indicates a local crystalline (hcp) motif.

Fig. 3(a) shows the cumulative probability distributions of φ_6^{local}, $\Pi(\varphi_6^{local})$, for the Gaussian and uniform packings. Opposed to the largely linear growth of $\Pi(\varphi_6^{local})$ for the uniform packing, $\Pi(\varphi_6^{local})$ increases exponentially towards unity for the Gaussian packing, where for the majority of particles (>80%) φ_6^{local} is larger than 0.8 and the average value of φ_6^{local} is as high as 0.88, indicating the prevalence of a distorted hcp motif. The overwhelming local crystalline order in the Gaussian packing is evident in the structural configuration of the packing (see Fig. 3(b)), conspicuous crystallized subdomains readily identified. Furthermore the global bond orientational order for the Gaussian packing also achieves a relatively high value, $\varphi_6^{global} \sim 0.78$, suggesting a propensity for a highly crystalline packing throughout or a collection of aligned partially crystallized domains rather a polycrystalline packing with a random distribution of phase orientation. In contrast with the highly ordered (both locally and globally) Gaussian packing, the uniform packing possesses only a moderate local bond orientational order with $\langle\varphi_6^{local}\rangle \sim 0.59$ as found in dense liquids (Steinhardt et al., 1983) and a trivial value of global bond orientational order, $\varphi_6^{global} \sim 0.022$, indicative of a typical amorphous packing (Schreck et al., 2011). Indeed the hcp motif can barely be recognized in the uniform packing (see Fig. 3(c)).

3.3. Contact normal fabric

A highly crystallized Gaussian packing entails substantial fabric anisotropy, or equivalently preferential microstructural orientations in terms of inter-particle contact normal directions (Hanifpour et al., 2015). Fig. 3(d) plots the directional distribution of inter-particle contact normal density, $\rho(\mathbf{n})$, in the Gaussian packing. As presumably a symmetrical pattern of contact-fabric emerges with six dominant orientations of the contact normal vectors, again manifesting an hcp crystallized structure. The amorphous uniform packing corresponds to an isotropic fabric, which is supported by the uniform azimuthal distribution of contact normal density as shown in Fig. 3(e).

To quantify the intensity of anisotropy, i.e. how scattered the directional distribution of contact normal is, we employ the fabric tensor widely used by the geomechanical community (Oda, 1982;

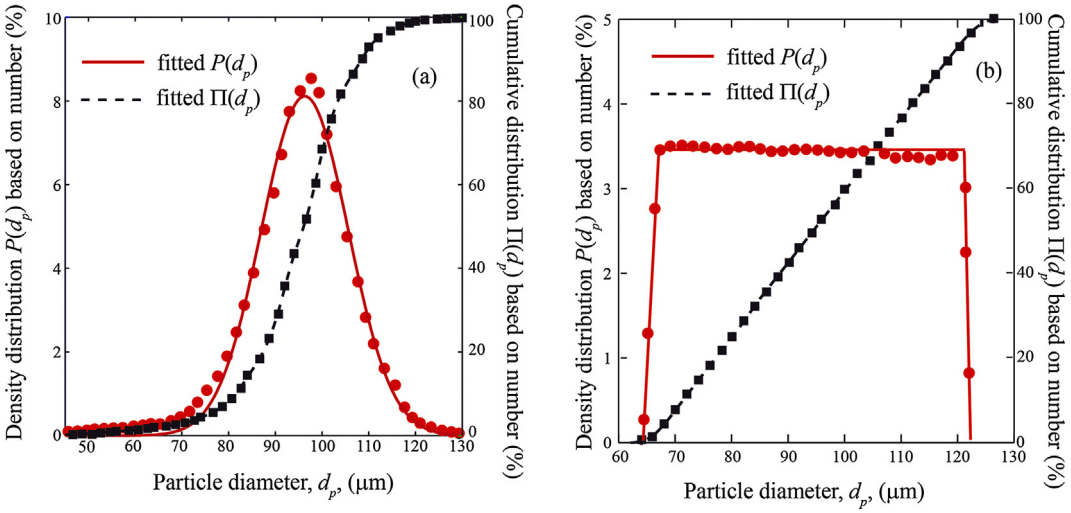

Fig. 2. Probability density ($P(d_p)$) and cumulative density ($\Pi(d_p)$) distributions of particle diameters in the Gaussian (a) and uniform (b) packings.

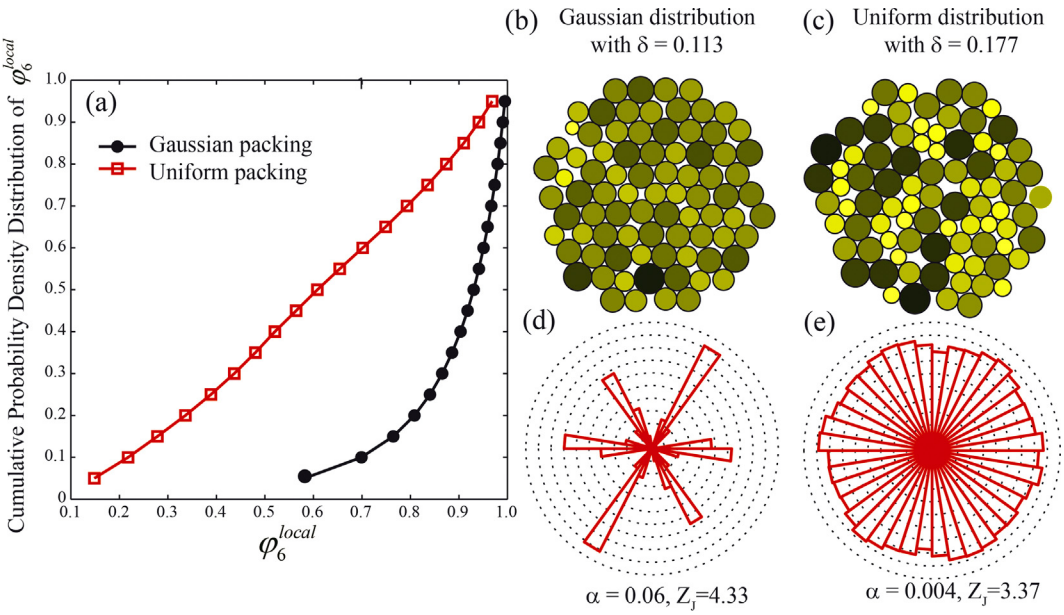

Fig. 3. (a) Cumulative probability distributions of φ_6^{local} in Gaussian and uniform packings. (b) and (c) configurations of particle arrangement in Gaussian (b) and uniform (c) packings. (d) and (f) directional distributions of contact normals in Gaussian (d) and uniform (e) packings.

Oda et al., 1985; Fu and Dafalias, 2011; Yang et al., 2016; Sun and Sundaresan, 2011; Vidyapati and Subramaniam, 2016)

$$\boldsymbol{F} = \frac{1}{N}\sum_{a=1}^{N} \boldsymbol{n}^a \otimes \boldsymbol{n}^a, \tag{4}$$

where N is the total number of contact normal vectors, $\mathbf{n}$, and $\otimes$ operation is the tensor product of the two vectors. The difference between the two principal components of the fabric tensor, $\alpha = F_I - F_{II}$, characterizes the intensity of anisotropy. $\alpha = 1$ means all vectors share the same direction and $\alpha = 0$ represent a uniform distribution across all directions. The amorphous uniform packing has a negligible value of α, $\alpha = 0.004$, one order of magnitude less than the crystallized Gaussian packing where $\alpha = 0.06$.

4. Computational procedure

4.1. Numerical model

The problem analyzed numerically in the present study is a 2D representation of the explosively driven particle jetting in three-dimensional cylindrical configurations used in experiment (David et al., 2012). Fig. 4 presents a numerical model for the 2D explosive dispersal of particle ring with a Gaussian packing structure. The model consists of a central circular FEM Lagrangian domain with the radius of R_{in} filled with explosives (TNT or PE4) and a surrounding particle ring made of quartz sand disks generated via the protocol introduced in Section 3.1. There are no inner and outer casings in our model. The left close-up inset in Fig. 4 shows how the outmost meshes in the explosive domains are refined to better conform to the circular edge. Likewise to ensure the inner and outer circular edges of the particle ring smooth enough, the innermost and outermost particle layers are comprised of substantially smaller particles with the average diameter of $\sim 0.6d_0$ (see the left and top close-up insets in Fig. 4). The drastic change of particle diameter from the innermost layer to the second layer whose average particle diameter restores the specified one yields several disordered adjacent layers. So does the particle arrangement adjacent to the outmost layer. But for the Gaussian packing the bulk of particles largely retains crystallized structure (see the close-up insets

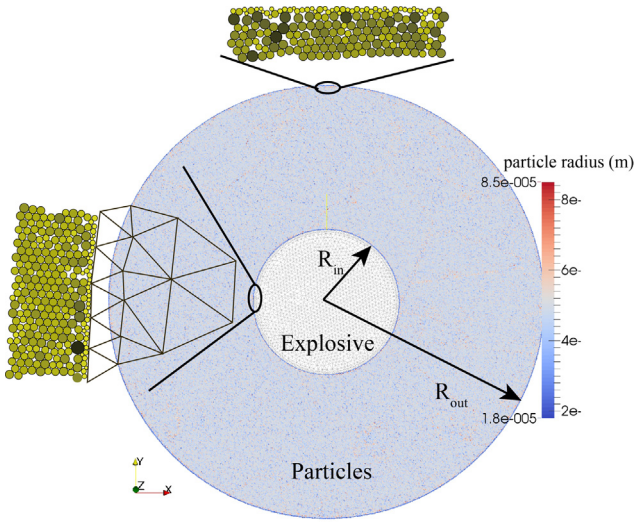

Fig. 4. Numerical model of explosive dispersal of 2D particle ring with a Gaussian packing structure. Insets: Close-up configurations showing the explosive meshes and particle arrangements adjacent to the inner (left inset) and outer (upper inset) surfaces of particle ring.

in Fig. 4). Material parameters used in DEM simulations are presented in Table 1.

Besides the microstructure of particle packing, we also investigate the influences of a variety of important parameters on the jetting formation, including the average particle diameter, the powder fill-to-burster charge mass ratio (F/B) and the type of explosive. Table 2 summaries the conditions of numerical tests performed in the present work. Note that we change the F/B ratio by varying the outer radius of the particle ring, R_{out}, while keeping the R_{in} unchanged, $R_{in} = 10$ mm.

The two-dimensional geometry has been widely used to simulate the detonation of spherical explosives and the explosive dispersal of particles (Balakrishnan, 2014; Mo et al., 2018a). Although the three-dimensional processes cannot be fully understood from the two-dimensional simulations. The underlying phy-

Table 1
Material properties of particles used in DEM. Here ρ_p, Y_p, ν_p, μ_p, ξ_n denote the solid density, Young's modulus, Poisson's ratio, sliding friction and normal damping ratio of particle, respectively.

material	ρ_p (kg/m^3)	Y_p (GPa)	ν_p	μ_p	ξ_n
Quartz sand	2560	72	0.27	0.3	0.3

Table 2
numerical conditions for the simulated tests.

Test no.	explosive	Particle number (10^6)	R_{out} (mm)	d_0 (μm)	Packing	F/B
1	TNT	1.81	30	38.4	Gaussian	11.09
2	TNT	0.29	30	95.7	Gaussian	11.05
3	PE4	0.29	30	95.7	Gaussian	11.33
4	TNT	0.545	40	95.9	Gaussian	20.6
5	TNT	0.53	40	95.6	Uniform	20.4
6	TNT	0.87	50	96.2	Gaussian	32.9

sics in terms of shock-particle interaction and mesoscale particle deformations revealed by the present two-dimensional simulations shed fundamental lights on understanding the three-dimensional processes.

4.2. Stress and strain fields obtained from DEM

One advantage of DEM is its capacity to construct the mesoscale strain rate and stress fields via grain-scale particle velocities and inter-particle contact forces (Zhu et al., 2007; Huang et al., 2010; Fu and Dafalias, 2011; Wang et al., 2013; Yang et al., 2016; Yongbo et al., 2016; Shi et al., 2017; Yuan and Shen, 2017 ;Zheng et al., 2017). Fig. 5(a) shows a typical particle velocity field in test no. 1 at $t = 4$ μs where particles are colored in proportion to the magnitude of their velocities. The instantaneous particle velocity field can be smoothed out with locally spatial averaging which gives an estimate of the continuum flow-field, $\mathbf{v}(\mathbf{r},t)$, where $\boldsymbol{r}$ are spatial coordinates of the bins used in the coarse graining. Here a set of 2D bins based on the (r,θ) polar coordinate system is employed for the coarse graining with the bin size $dr = 5$ or 10 d_0, $d\theta = \pi/90$. Fig. 5(b) shows a coarse-grained velocity field with the bin size $dr = 5\ d_0$ which retains the exact features evident in Fig. 5(a). Most prominent feature in Fig. 5(a) and (b) is the non-uniform azimuthal profile of velocity, specifically velocities at the corners of the undulated shock front are substantially higher than those in the neighboring areas. The strain rate tensor $\mathbf{G}$ is then deduced for each bin by

$$\boldsymbol{G} = \frac{1}{2}\left(\nabla \boldsymbol{v} + \nabla \boldsymbol{v}^T\right), \tag{5}$$

where the exponent T refers to the transpose matrix.

The stress tensor σ for each bin is computed as

$$\boldsymbol{\sigma} = \frac{1}{S}\sum_{k=1}^{N}\sum_{l=1}^{N_k} \boldsymbol{F}_{kl} \otimes \boldsymbol{r}_{kl}, \tag{6}$$

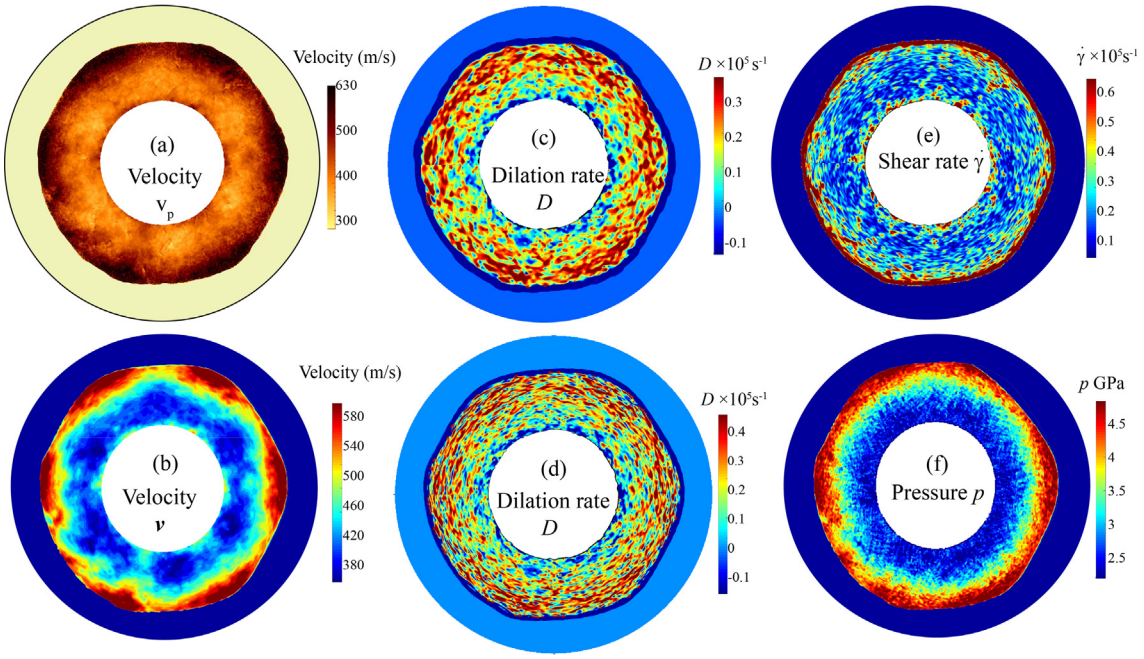

Fig. 5. (a) Particle velocity field. (b) Coarse-grained velocity field with the bin size $dr = 5d_0$. (c) Coarse-grained dilation rate field with the bin size $dr = 10\ d_0$. (d–f) Coarse-grained dilation rate field (d), shear rate field (e) and pressure field (f) with the bin size $dr = 5d_0$. All the plots correspond to the particle ring in test no. 1 at $t = 4$ μs.

where $\mathbf{F}_{kl}$ is the contact force between the two particles k and l in contact, $\boldsymbol{r}_{kl}$ is the contact vector pointing from the center of particle k towards the center of particle l, N_k is the number of neighbors of particle k, N is the particle number in the computational bin, S is the area of the bin. Note that the present 2D stress is a force per unit length and not a force per unit area.

Both strain rate and stress tensors, $\mathbf{G}$ and σ are decomposed into an isotropic part and a deviatoric part:

$$\begin{aligned} \boldsymbol{G} &= D\boldsymbol{I} + \boldsymbol{G_d} \\ \boldsymbol{\sigma} &= -p\boldsymbol{I} + \boldsymbol{\sigma_d} \end{aligned}, \tag{7}$$

where $\mathbf{I}$ is the unit tensor, $D = 1/2tr(\boldsymbol{G}) = 1/2\mathrm{div}\boldsymbol{v}$ is the dilation rate of the 2D particle flow, $\mathbf{G}_\mathrm{d}$ is the shear rate tensor, p is the pressure, and σ_d is the shear stress tensor. The shear rate $\dot{\gamma}$ is related to the deviatoric part of $\mathbf{G}$ as defined as

$$\dot{\gamma} = \left[\frac{1}{2}tr\left(\boldsymbol{G_d^2}\right)\right]^{1/2}. \tag{8}$$

Fig. 5(c) and (d) shows the coarse-grained dilation rate fields, D, corresponding to the velocity field plotted in Fig. 5(b) using two sets of bins with $dr = 10d_0$ and $dr = 5d_0$, respectively. No fundamental differences can be identified between Fig. 5(c) and (d). Thus the fine mesh, $dr = 5d_0$, is to be employed in the henceforth coarse graining procedure. The calculated coarse-grained shear rate field, $\dot{\gamma}$, as well as the pressure field, p, are presented in Fig. 5(e)–(f), respectively.

Two striking features can be readily detected from the strain rate and pressure fields. First is the hexagonal shaped shock front. The undulation of the shock front is indicative to the highly ordered microstructure in the Gaussian packing which would be discussed in Section 5.4. Second is the meso-scale heterogeneities intrinsic to the dilation and shear rate fields (see Fig. 5(c)–(e)). The characteristic length scale of heterogeneity associated with the radial variation of the dilation or shear rates is of the order of $10^1 d_0$ irrespective of the bin size.

5. Results and analysis

5.1. Multiple wave interactions with particles

Extensive experimental observations via either high-speed photography or radiography all elaborate that the formation of the explosively driven particle jetting occurs on the timescale of shock interaction (Milne et al., 2010; Milne et al., 2014; Ripley and Zhang, 2014; Frost et al., 2017a; 2017b; Frost, 2018; Loiseau et al., 2018; Pontalier et al., 2018). Thus it is of essence to understand how the particle layers evolve while being subjected to multiple shock and rarefaction waves related with the detonation of the confined explosive. In this section, we describe a typical shock-particle interaction scenario occurring in test no.1. Fig. 6(a) plots the trajectory of the pressure front, R_p, delimiting the stressed and stress-free particles, as well as the outer boundary of the compact particle layers, R_comp, whose packing fraction is close to that of the densest random close packing ($\phi \sim 0.84$).

When a high-pressure gas is suddenly released as the detonation wave consumes all central explosive, a primary blast wave (denoted by PSF in Fig. 6(a)) propagates outward into the particles. In cylindrical and spherical geometries, alongside the outward-moving blast wave, a rarefaction wave moves inward into the detonation gases and over-expands the flow, resulting in a secondary shock (denoted by SSF in Fig. 6(a)) (Balakrishnan, 2014). The secondary shock is weak at early times and is driven outward by the rapidly expanding gases from the center of the explosion. However, in due course this secondary shock strengthens due to the coalescence of pressure pulses. An inward traveling rarefaction wave (denoted by RW in Fig. 6(a)) ensues the reflection of the primary shock upon the external boundary of the ring at $t = 5$ μs. The rarefaction wave is arrested by the secondary shock front $t = 9$ μs. The advancing secondary shock progressively rebuilds the compressive stresses in the released particles.

Opposed to the immediate release of compressive stresses, the bulk of particles in the wake of the rarefaction wave except the outermost layer remain tightly packed for the time being although

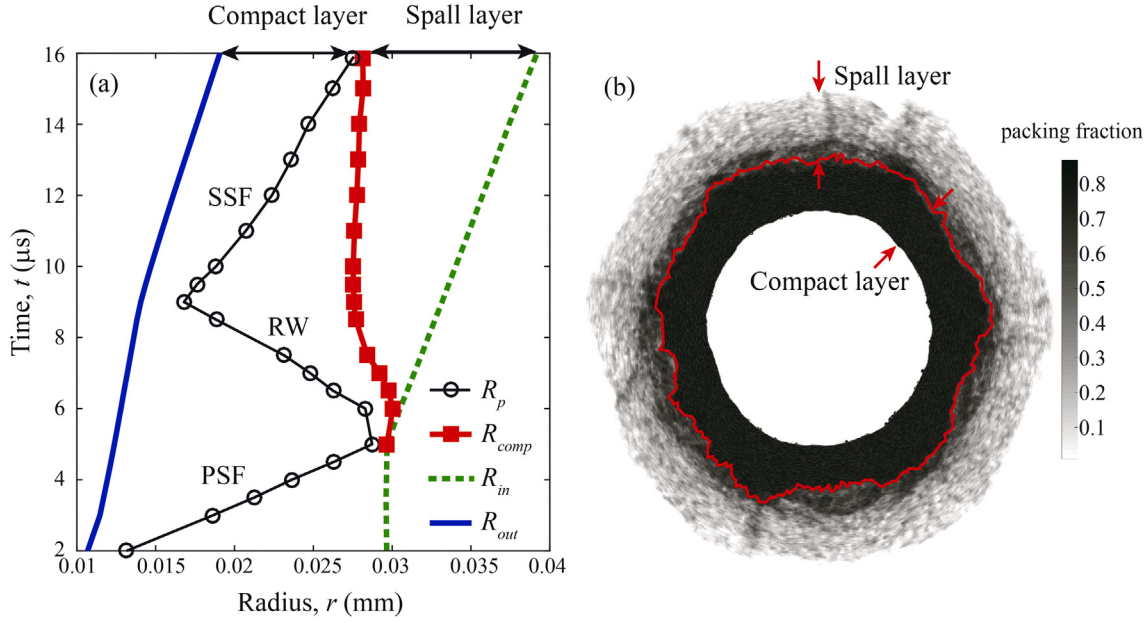

Fig. 6. (a) trajectories of the inner and outer radii of the particle ring in test no.1, R_in and R_out, the pressure front, R_p and the boundary delimiting the inner compact layer and outer dilute spall layer, R_comp. Here PSF, RW and SSF refer to the primary shock front, the rarefaction wave and the secondary shock front, respectively. (b) Coarse-grained packing fraction field of the explosive dispersed particle ring at $t = 17$ μs in test no.1. Note that the instantaneous particle ring is composed of an inner compact band with packing fraction $\phi \sim 0.84$ and an outer spall layer with $\phi < 0.6$.

the inter-particle stresses have been released. Analogous to the spall cavitation in liquid or metallic glasses the particle erosion initiated by the rarefaction wave takes a while to complete, leading to the boundary delimiting the compact ($\phi \sim 0.84$) and spall ($\phi < 0.6$) layers, R_{comp}, significantly lagging behind the rarefaction wave. At $t \sim 16$ μs the inward progress of particle erosion is thwarted by the outward-travelling secondary shock (see Fig. 6(a)). As a result, the initially coherent particle ring is well disintegrated into an inner compact particle band ($\phi_{comp} \sim 0.84$) with an undulated envelope and a dilute spall layer ($\phi_{spall} < 0.6$) as indicated in Fig. 6(b). The velocity of the inner compact band exceeds the spall particles due to the continuous propelling of the detonation gases so that the inner band gathers up the spall particles until the velocity surplus of the inner band is exhausted. This matter would be elaborated in Section 5.6.

5.2. Shock compaction of particles

Fig. 5(c)–(f) shows the deformation pattern in the shocked particles prior to the emergence of the secondary shock in terms of dilation rate and shear rate fields. Except a thin layer with the thickness of $5d_0$ attached to the shock front which undergoes intense compression, the bulk of particle ring exhibits an intricate mosaic pattern of dilation with interwoven expansion and compression on the length scale of dozens of particle size (see Fig. 5 (b) and (c)). So does the shear rate field as shown in Fig. 5(e). Note that the features in the dilation rate or shear rate fields form a pattern of concentric rings with rumpling edges.

With the advent of the secondary shock front, the innermost layers are re-compressed and re-accelerated as indicated by the increments of pressure and velocities in the innermost layer (see Fig. 7(a) and (b)). In contrast with wavy-like concentric circle patterns of dilation and shear rate fields induced by the primary shock (Fig. 5(c) and (e)), the deformation of the innermost layers sustained by the secondary shock is dominated by profuse localized compaction/shear bands which emanate from the inner perimeter of the ring, spiral outward and fade away (see Fig. 7(c) and (d)). The crossing of clockwise compaction/shear bands and the counter-clockwise counterparts gives rise to a grid pattern. The localized shear banding persists in the expanding inner compact particle band as will be discussed in Section 5.4.

5.3. Reflection of the rarefaction wave

The rarefaction wave reflected back into the particles is soon headed off by the secondary shock, only a thin layer of particles being stripped away. At $t = 10$ μs the secondary shock front delineating the boundary of stressed particles (denoted by the white hexagon in Fig. 8(a)) is well inside the external boundary of the compact particle layer (denoted by the black circle in Fig. 8(a)). The radius of the compact layer, R_{comp}, coincides with the first kink of the ϕ vs r curve and the second kink of the v vs r curve (Fig. 8(c)), while the secondary shock brings out the end-raising of the v vs r curve. The outward-travelling secondary shock front is met with the inward-shrinking boundary of compact band at $t = 20$ μs. Afterwards a dilute spall layer is pulled away from the inner compact band (denoted by the white hexagon in Fig. 8(b)).

Fig. 8(a) shows the dilation rate field in test no.1 at $t = 10$ μs. The spallation of the particle layer delineated by the secondary shock and the compact band boundary is dominated by the heterogeneous, localized dilation pattern rather than the homogeneous, diffuse dilation mode. The close-up inset in Fig. 8(a) reveals a network-like dilation pattern in the particles which are about to be eroded away. Actually this heterogeneous dilation pattern bears

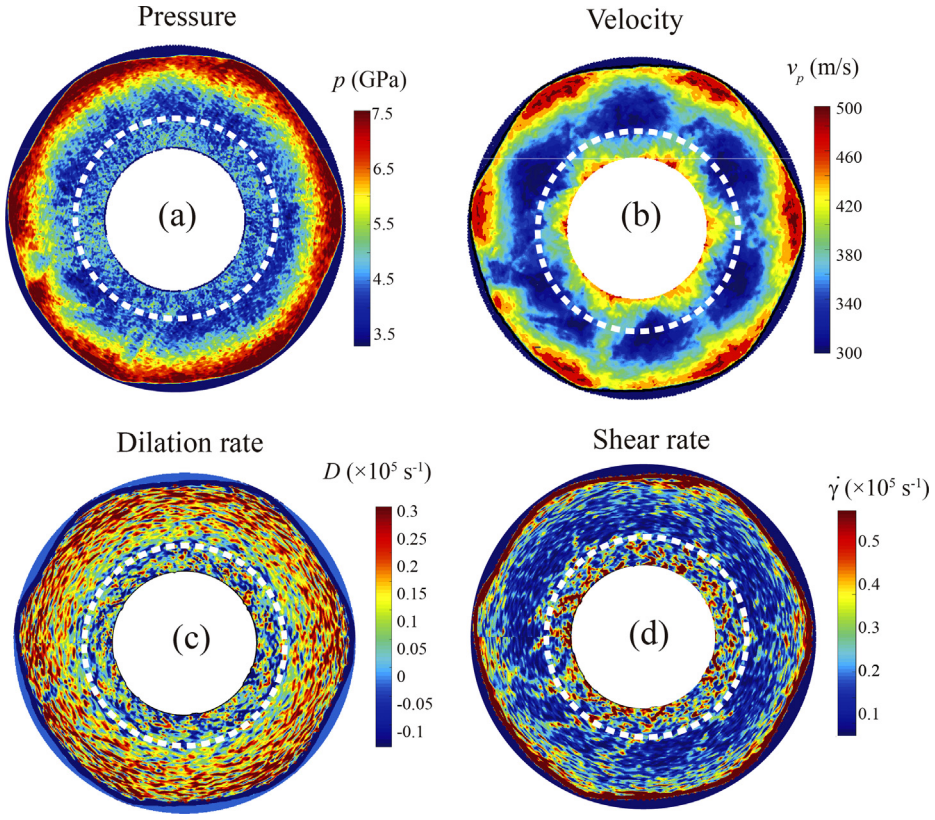

Fig. 7. coarse grained fields of pressure (a), velocity (b), dilation rate (c) and shear rate (d) in the shocked particle ring at $t = 5$ μs in test no.1. The dashed circles denote the influence areas of the secondary shock.

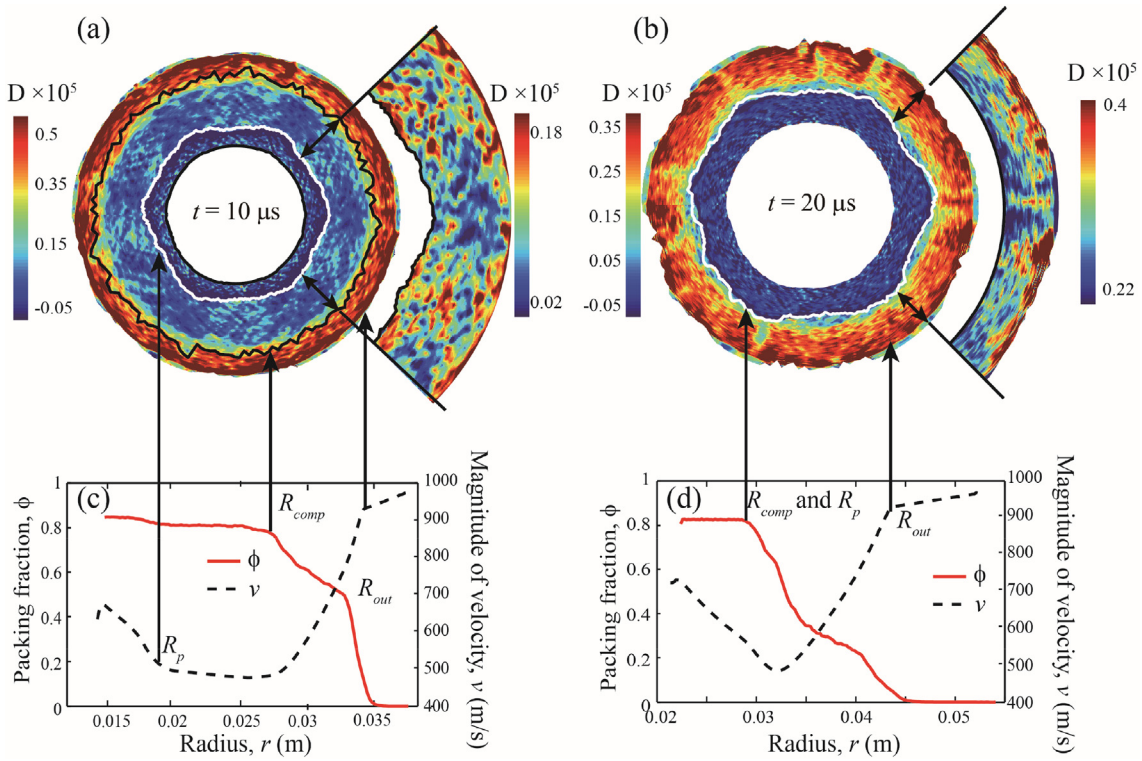

Fig. 8. Profiles of the dilation rate in the particle ring at t = 10 (a) and 20 μs (b) in test no.1. The radial variations in packing fraction and particle velocity at t = 10 (c) and 20 μs (d). The hexagonal shaped white circles in (a) and (b) denote the secondary shock fronts. The black circle in (a) represents the boundary between the loose and compact particles.

the resemblances to the intersecting curvilinear compaction/shear bands seen in the particles recompressed by the secondary shock (Fig. 7(c) and (d)). The dilation in the newly born spall layer (see the inset in Fig. 8(b)) also displays a heterogeneous pattern analogous to that shown in the inset in Fig. 8(b). As a result, the density distribution in the spall layer is significantly non-uniform. Particles undergone relatively weak dilation are prone to stick together, becoming the nuclei of the particle agglomerates. By contrast, particles undergone substantial dilation are dispersed both radially and laterally. Due to the lateral confinement, the dispersed particles are likely to coalescence into the adjacent particle clusters. The spall particles consequently forms a large number of particle clusters instead of a particle cloud consisting of constituent grains.

Fig. 9 presents the snapshots of shock dispersed ring in test no.1 at t = 20 and 100 μs. The fuzzy spall layer at t = 20 μs evolves into a filamentary ray-like structure at t = 100 μs. A set of regularly

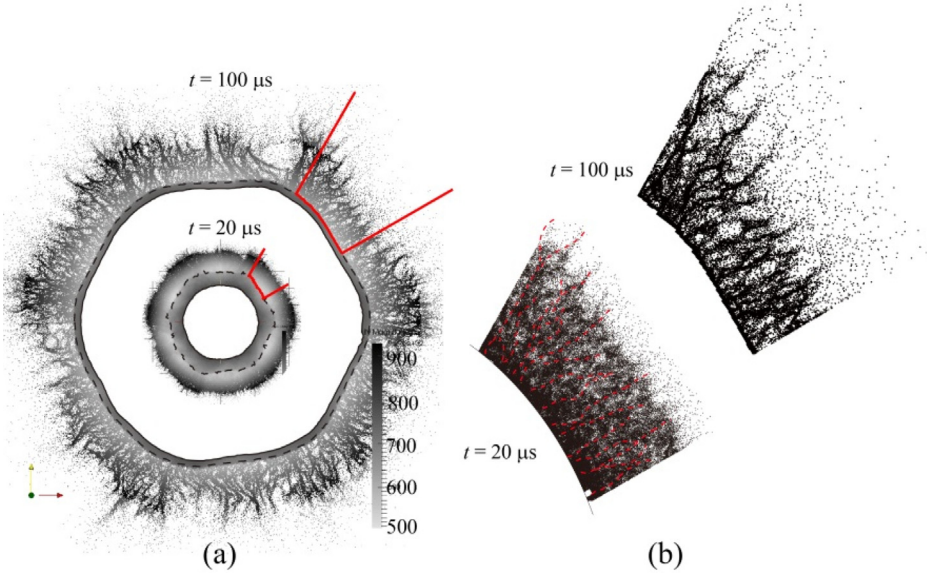

Fig. 9. (a) Superimposed snapshots of the shock dispersed ring in test no.1 at t = 20 and 100 μs. (b) The zoom-out snapshots of the ring segment outlined in (a) at t = 20 and 100 μs. The red dashed lines superimposed on the snapshot of the ring segment at t = 20 μs represent the skeleton of coherent jets identified from the snapshot of the same ring segment at t = 100 μs. (For interpretation of the references to colour in this figure legend, the reader is referred to the web version of this article.)

spaced side-branched spikes can be recognized from the zoomed in snapshot of part of the spall layer shown in Fig. 9(b), which protrude outwards with spacing of dozens of particle size. Superimposing the particles spikes at $t = 100$ μs (illustrated by the red dashed line in the bottom panel of Fig. 9(b)) onto the spall layer at $t = 20$ μs suggests the coincidence between the incipient particle agglomerates and the well-defined particle jets at later times. The radiographs of the particle shells subjected to the central explosion record a number of fine structural features appearing on the surfaces of particle shells during the first dozens of microseconds, suggesting the incipient failure of compressed particle layers may well be caused by the tensile loading from the rarefaction wave (Milne et al., 2014; Frost et al., 2017a). Indeed our FEM-DEM simulations support this argument. During the first dozens of microseconds, a large number of minor jets are well formed spanning the whole external perimeter of the ring. More importantly the formation of external minor jets is found to be caused by the heterogeneous dilation of spall layers, which in turn is rendered by the localized compaction mode in the shock compacted particles.

5.4. Deformation mode and fracture of inner compact particle band

Compared with the outer spall layer, the inner compact particle band retains the maximum packing fraction while rapidly expanding outwards for a relatively long time (see Fig. 10). As shown in Fig. 10, the coarse-grained packing fraction in the compact inner particle band only varies within a narrow range of 3 percentages without noticeable localized dense or loose packed patches. Accordingly the azimuthal variations of radially averaged packing fraction in the compact inner particle bands fluctuate randomly and don't have a consistent pattern over time (see Fig. 10(b)). It has long been suspected that it is the localized densification during the shock interaction that is responsible for the fragmentation of the particle shell and the ensuing particle jetting (Frost et al., 2017a, 2017b; Loiseau et al., 2018). Nevertheless our simulations which don't take into account of thermal effects find that the shock compaction doesn't necessarily lead to the non-trivial localized densification. Whether or not the "sintering" could occur and eventually cause the localized densification will be discussed in Section 6.2.

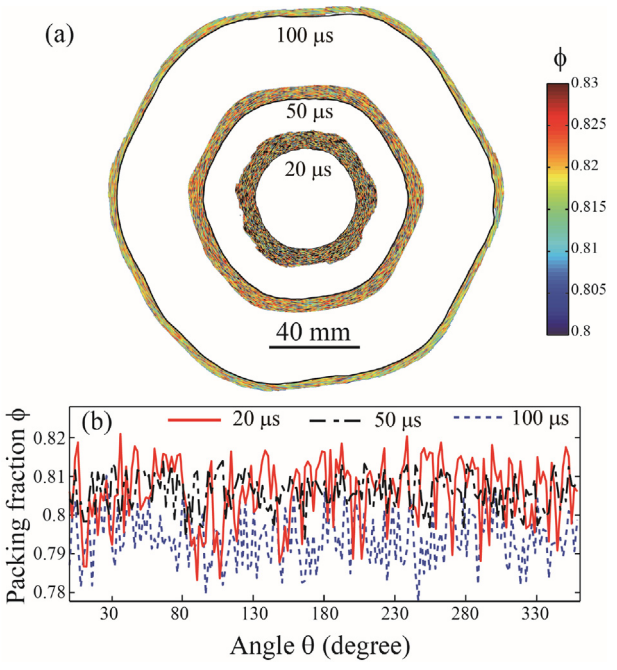

Fig. 10. (a) superimposition of the profiles of packing fraction in the inner compact particle band at different times. (b) Azimuthal variations of the radially averaged packing fraction in the inner compact particle band at different times.

The deformation in the expanding inner compact particle bands in all tested cases are shown in Fig. 11 in terms of shear rate and dilation rate fields. Again profuse shear localization can be seen for all of them. The shear-band configurations for these six particle rings are schematized in illustrations below the shear rate fields. In the inner radius region, all shear bands follow roughly an angle of 45° with the radial direction, corresponding the maximum shear direction. The inclination angle of the shear bands with respect to the radial direction increases as the trajectory moves towards the outer radius regions. The angle is determined by the magnitudes of the principal stresses and shear strength, and can be predicted from the Mohr-Coulomb flow criterion. Since the shear strength of granular materials is a function of the pressure, it is expected that the variation in angle is associated with the change in principal stresses from the inner radius to the outer radius. Note that the shear banding pattern which is well established when the inner compact particle ring is formed persists throughout the expansion of the ring in terms of the position of shear bands.

Both clockwise and counterclockwise shear bands can be identified from all studied cases. There exist six groups of the clockwise and counterclockwise shear bands in particle rings composed of the Gaussian packings (see Fig. 11(a)–(d) and (f)). The grouping is indicative of cooperative material motion and self-organization among the bands. What is worth noting is that all the external boundaries of the inner compact bands in these five cases are hexagonal shaped and the six well-separate groups of shear bands dwell within the edge segments between the corners of undulated bands. By contrast, it is hard to distinguish the groups of shear bands in the particle ring composed of the uniform packing (see Fig. 11(e)). Clockwise and counterclockwise shear bands are distributed fairly evenly around the inner perimeter in the inner compact band whose outer boundary remains circular. Correlations between shear strain and positive volumetric strain are evidence of shear dilation (see Fig. 11(g)–(i)), a well-established feature of deformation in granular materials (Alsiny et al., 1992; MacMinn et al., 2015).

Since the expansion of detonation gases is modeled by the Lagrangian meshes confined by the particle ring in the present work, the localized failure of the particle ring causes the severe distortion of the internal explosive mesh, leading to the breakdown of the simulation. Although the eventual fragmentation of the expanding particle ring cannot be properly simulated yet, the emergence of a network of spiral shear bands that span the entire system at the first dozens of microseconds is consistent with the synthesized crack pattern derived from the radiographs of the spherical particle shell dispersed by the central explosion taken at the same time-sale (Milne et al., 2014). The shear dilation thus is very likely to be the precursor to the fragmentation of the expanding particle ring. Actually shear failure characterized by the shear bands following logarithmic spirals has been found to be responsible for a variety of radial dilation and hydraulic fracture, such as the fracture of thick-walled dense sand hollow cylinders in cavity inflation experiments (Bohloli and de Pater, 2006; Alsiny et al., 1992), and the failure of thick-walled granular SiC hollow cylinders subjected to the convergent blast waves generated by the detonation of the surrounding explosive (Shih et al., 1998).

The areas in which the clockwise and counterclockwise shear bands are grouped are more prone to the failure since the shear dilation therein is most intense. Frost et al. found that a short glass bead ring which is close to the two-dimensional configuration studied here is dispersed into particle jets with the number less than ten (David et al., 2012). The structural order of the particle packing in the experiment is unknown. But the experimental

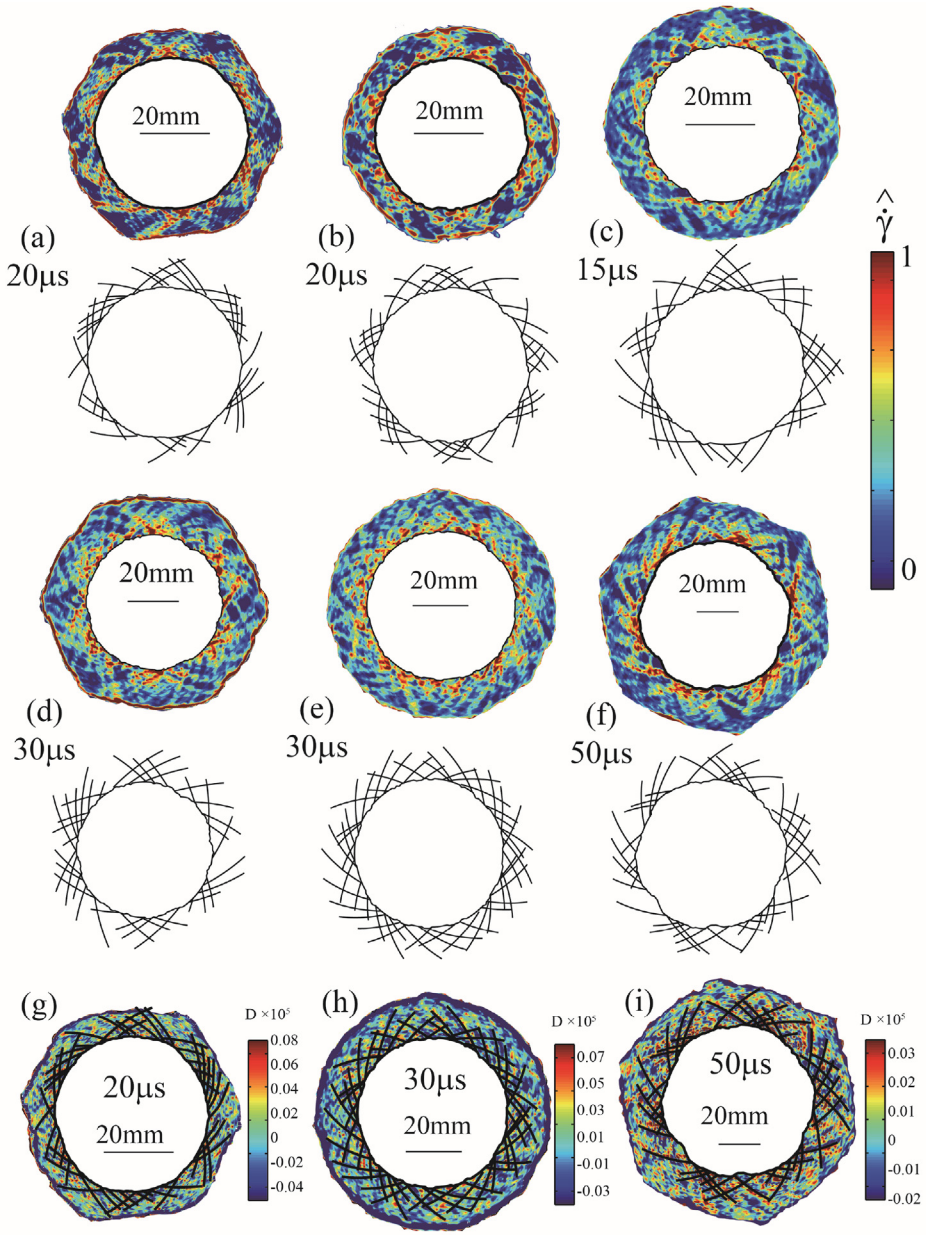

Fig. 11. (a)–(f) Top panels: shear rate fields in the inner compact particle bands in test No. 1–6, respectively; bottom panels: illustrations of shear-band configurations corresponding to the upper shear rate fields. (g)–(i) Dilation rate fields in the inner compact particle bands in test No. 1, 5 and 6, respectively, superimposed by the corresponding shear-band configurations represented by the black curves.

observed number of jets falls into the range delimited by the numbers of shear band groups in two extremes of the structural order spectrum. Near the high structural order limit, the particle ring with global crystalline structure has six groups of shear bands. In the low structural order limit, the particle ring with amorphous structure has around tens of groups of shear bands.

5.5. Influence of the structural order on the deformation mode

The grouping of the clockwise and counterclockwise shear bands substantially changes with the structural order of the particle packing as discussed in Section 5.4. Actually the grouping of shear bands is closely associated with the distinctive velocity field that varies with structural order (see Fig. 12(a)–(c)). The velocity fields shown in Fig. 12(a)-(c) are characterized by a petal-like meso-scale structure that corresponds to spiral shear bands (MacMinn et al., 2015). Each "velocity petal" represents a group of particles that move faster than their neighbors, implying that the edges of each petal are bands of localized shear failure.

In the hexagonal shaped inner compact bands which have global crystalline structures, the small "velocity petals" coalesce into six large "velocity petals" which point towards the corners of the undulated external boundary of band. Actually the radially averaged velocity fluctuates azimuthally in concert with the outer radius of the particle band (see Fig. 12(d) and (f)). Accordingly there exist six groups of clockwise and counterclockwise shear bands in between these six large "velocity petals". On contrary, in the annular inner compact band with amorphous structure, a large number of small "velocity petals" are regularly distributed around the inner perimeter and overlap with each other. The coalescence of small petals occurs in a rather random and cascading manner. Instead of a handful of conspicuous large "velocity petals",

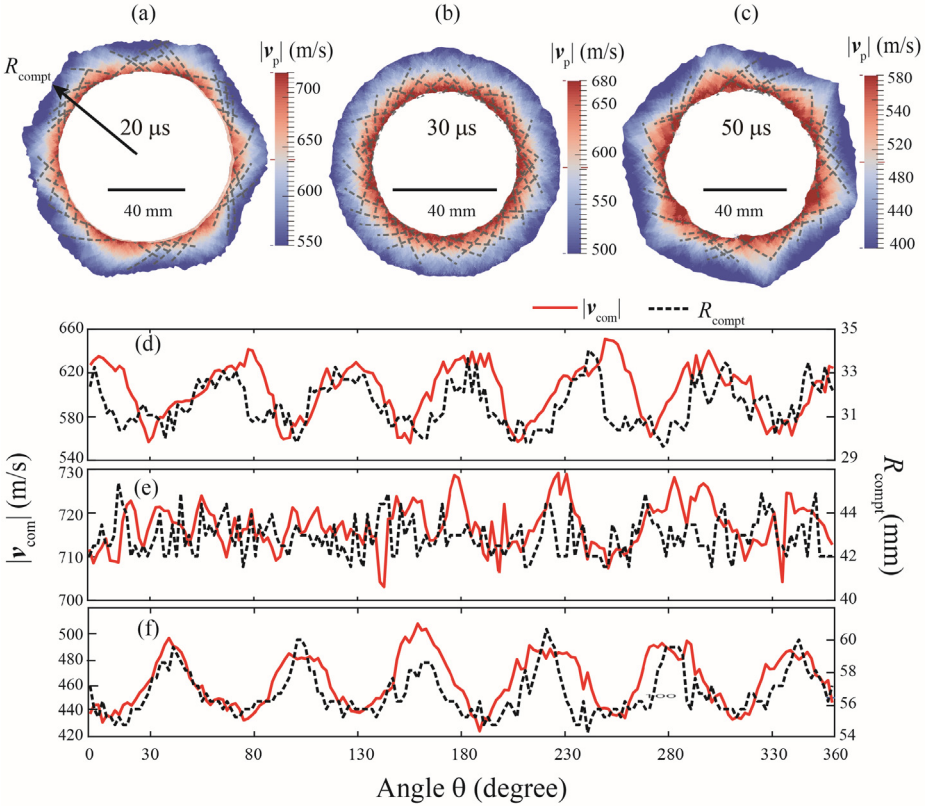

Fig. 12. Velocity fields in the inner compact particle bands in test no. 1 (a), 5 (b) and 6 (c), superimposed by the corresponding shear-band configurations represented by the black curves. (d)–(f) Azimuthal variations in the radially averaged velocity and outer radii of the inner compact particle bands in test no. 1 (d), 5 (e) and 6 (f).

the velocity field in the amorphous inner compact band exhibits dozens of moderate sized "velocity petals" as indicated by the short-wave fluctuation with small magnitude in the azimuthal variation of the radially averaged velocity (see Fig. 12(e)). As a result, there emerge much more groups of shear bands which are not well separate.

In the hcp crystalline packings, momentum is transmitted more quickly and efficiently along the six preferential contact directions. Thus as expected the initially circular primary shock front soon evolves into a hexagonal-like envelop with the six corners aligned with the preferential contact directions (see Fig. 13a)). Subsequently the shape of the rarefaction wave is the inversion of the primary shock front, and the secondary shock front resembles the primary shock front (see Fig. 13(a)). The external boundary of the inner compact particle band formed by the secondary shock also retains the hexagonal-like undulated shape analogous to the primary shock front (see Fig. 13(a)). So does the azimuthal variation in the radial velocity as corroborated by Fig. 12(d). By contrast, there are no noticeable preferential contact directions in the amorphous particle packings (test no.4). Accordingly the primary shock front, the rarefaction wave, the secondary shock front, as well as the external boundary of the inner compact particle band largely

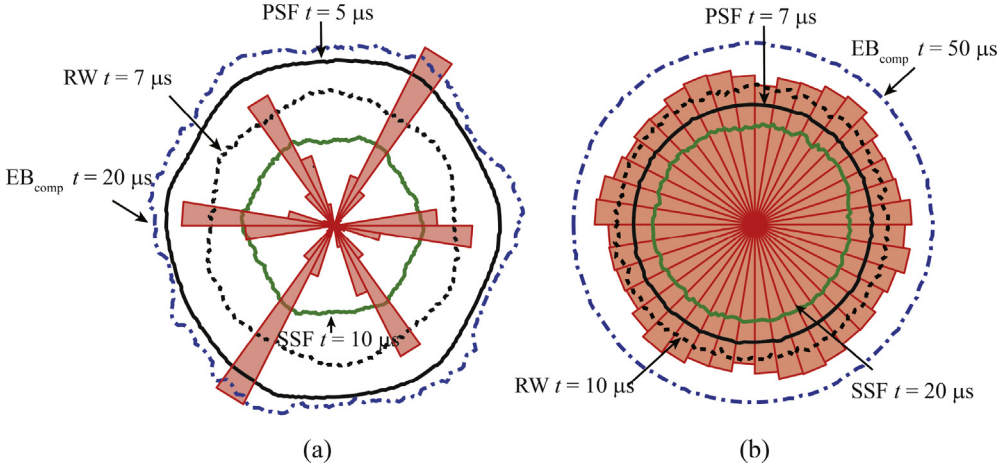

Fig. 13. Envelops of primary shock front (PSF), rarefaction wave (RW), secondary shock front (SSF), external boundary of compact inner band (EB_{comp}) in the test no.1 (a) and no.4 (b) superimposed by the corresponding rose diagram of contact normal.

remain circular (see Fig. 13(b)), indicating no distinguishable and persistent pattern in the velocity profile.

5.6. Degradation of dual particle jetting to single jetting

When the spall layer is pulled away from the inner compact particle band, the minor jets in the spall layer spawned by the particle clustering travel outward ballistically. Meanwhile the inner compact particle band propelled by the detonation gases continues to accelerate outwards. The accelerating inner compact particle band gathers up the spall particles in its path until there is no velocity surplus between the inner compact band and spall particles. Fig. 14(a)–(d) plots the variation of the fraction of particle number in the inner compact particle band alongside the velocity variations of the compact and spall layers in four typical tested cases. For test no. 1 (see Fig. 14(a)), as the expanding velocity of the inner compact particle band converges to a steady value, the fraction of particle number in the band, N_{compt}/N, ceases to increase. In the end about 70% of particles are entrained into the inner compact band.

If the inner compact band entrains all the spall particles, only internal jets caused by the fragmentation of the inner compact band survive. The dual jetting then is to degrade into a single jetting. In this scenario, the expanding velocity of the inner compact band eventually exceeds that of the spall layer as shown in Fig. 14 (b) and (c). A variety of parameters could play a role in the transition of the jetting mode, such as the type of explosive, F/B ratios, etc. Employing stronger explosive, such as replacing TNT with PE4, the velocities of the spall layer and inner compact band are both increased. But the inner compact band gains much larger momentum from the secondary shock due to the detonation gases with much higher pressure so that all spall particles eventually is engulfed by the inner compact band (see Fig. 14(b)). With the increased F/B ratio, the velocities of the spall layer and inner compact band are both reduced. But the influence of F/B ratio on the spall layer is much stronger, whose velocity is significantly reduced due to the stronger dissipation of the primary shock energy and the weakened rarefaction wave. The contribution of the secondary shock front driven by the expansion of detonation gases to the velocity of the inner compact band is barely changed with F/B ratio. Thus the inner compact bands in the cases with high F/B ratio (test no. 3–6) catch up the spall layer and gather up all the spall particles which have substantially reduced velocity (see Fig. 14(c) and (d)). The particle diameter and packing structural order studied in the present work cannot alter the jetting pattern. In all tested cases, only particle rings with F/B ~ 11 and TNT as explosive (test no. 1 and 2) retain the dual particle jetting patter. Only internal particle jets survive in other test cases.

Milne devised an engineering model to predict the velocity of porous shells, which corrects the Gurney theory to take account of porosity and bulk density effects (Milne, 2016). In the cylindrical geometry, the shell velocity V is calculated by

$$V(M/C,\rho_0,\phi) = V_g\left(\frac{M/C}{\alpha(\rho_0)}\right)\cdot F\left(\phi,\frac{M}{C}\right) \tag{9}$$

$$V_g(M/C) = \sqrt{2E}\left(\frac{M}{C}+0.5\right)^{-0.5} \tag{10}$$

$$\alpha(\rho_0) = 0.2\rho_0^{0.18} \tag{11}$$

$$F\left(\phi,\frac{M}{C}\right) = 1+(0.162\exp(1.127\phi)-0.5)\cdot\log_{10}\left(\frac{M}{C}\right) \tag{12}$$

The calculated shell velocities by Eqs. (9)–(12) for test no. 1, 3, 5, 6 are 754, 910, 581 and 459 m/s, respectively. The simulated velocities of inner compact particles bands in the corresponding tests are 720, 1050, 620 and 500 m/s, in well agreement with the theoretical predictions.

The dispersal velocity is the result of the momentum transfer from the blast waves to particles. The pattern of shear banding manifests the grain-scale packing structures. The consistency

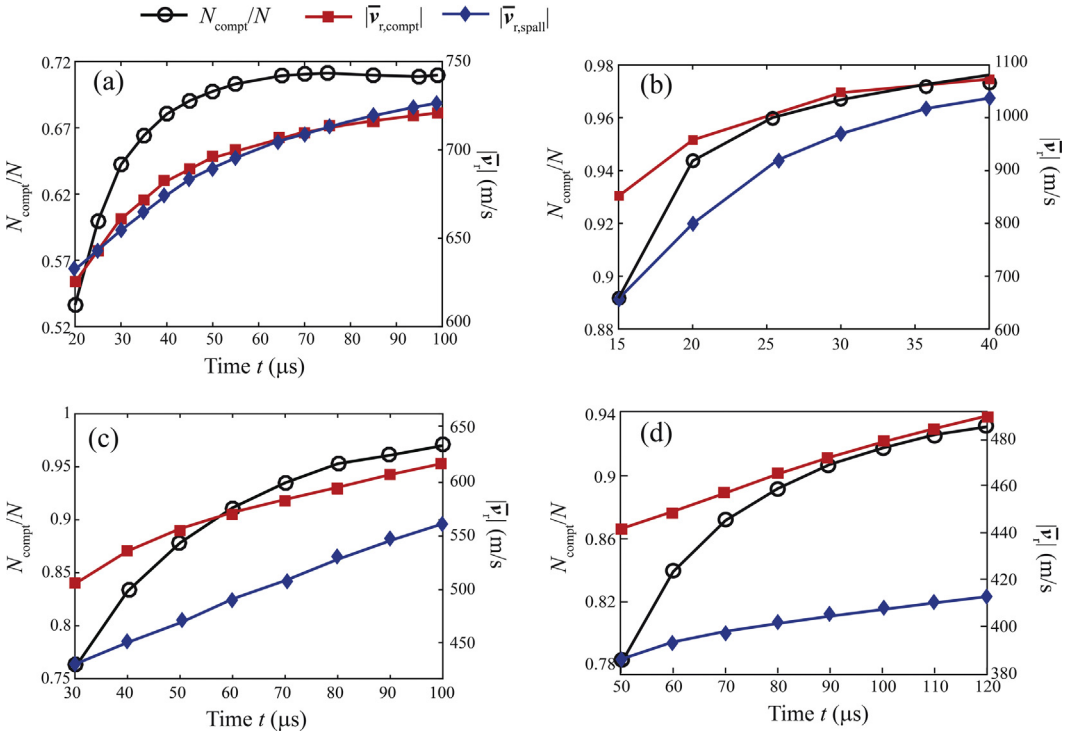

Fig. 14. Variations in average velocities of inner compact bands and spall layers, $|\bar{v}_{r,compt}|$ and $|\bar{v}_{r,spall}|$, as well as the fraction of particle number in inner compact band, N_{compt}/N, for test no. 1 (a), no. 3 (b), no. 5 (c) and no. 6 (d).

between our simulations and experiments in terms of macroscopic velocity and grain-scale instability pattern suffices to validate our simulations.

6. Discussion

6.1. Jetting mechanism

Previous experimental studies argue that it is a certain form of shock consolidation (sintering) resulted from the primary shock interaction with particles that leads to the brittle fracture of the particle shell upon the release of the rarefaction wave (Loiseau et al., 2018; Frost et al., 2017b; 2017a). This hypothesis is schematized in Fig. 15. Although the consolidated aluminum fragments collected after the trial (Frost et al., 2017a) seem to support the shock induced sintering (particle bonding), the applicability of this model across a wide range of particle materials, particularly the ceramic and metals with high melting temperature, requires more rigorous examination.

The direct observation of the shock interaction with particle packings and the full-scale postmortem analysis are both prohibitive for the explosive dispersal of particle shells. But a series of thick-walled cylinder experiments carried out by Shih et al. (1998) two decades ago may well shed some fundamental insights in this regard. In the experiments, the granular SiC hollow cylinders were squashed radially by two consecutive convergent explosive shock waves in a collapsing cylinder geometry. The tubular cavity of the SiC hollow cylinder was filled by a central copper rod during the densification of the first shock wave. A cylindrical orifice was then drilled in the center of the copper insert. The densified SiC hollow cylinder then underwent a second explosive event and collapsed the central orifice. Under the superimposed confinement pressure, Shih et al. (1998) found the SiC cylinders achieved approximately 83–88% of theoretical density during the first explosive event, while the density was reduced to 63–78% of theoretical density after the second explosive events during which the SiC cylinder was allowed to deform. Hence in the divergent shock configuration without confinement as studied here, it is almost impossible to expect that the divergent blast wave can compact particles to near solid density.

Shih et al. (1998) did found a thin layer (5–20 μm) of well-bonded materials within shear bands and attributed this strong particle bonding to the combined effects of intense plastic deformation and heating, during the shear localized event, under the influence of high superimposed confining pressure. But the "sintering" within shear bands only occurred in the fine and medium particles with the average particle diameter of 0.4 and 3 μm, respectively. In the coarse powder specimens ($d_0 \sim 50$ μm), the shear localization process primarily involves the particle comminution and rearrangement of the comminuted particles rather than the particle bonding. Besides the calculated heating time within the shear bands which undergo intense plastic deformation is of orders of dozens of microseconds, and the temperature rapidly decreases after it peaks.

In general there are three primary conditions required by the shock induced material bonding, namely the micro to submicro particles, the severe plastic deformation within the shear bands, and a loading time at least of dozens of microseconds. Except a few exceptions, the particle size used in the tests of explosive dispersal of particles is mostly of the orders of 10^1–10^2 μm (Milne et al., 2010; Ripley et al., 2011; David et al., 2012; Xue et al., 2013; Milne et al., 2014; Ripley and Zhang, 2014; Frost et al., 2017a, 2017b; Loiseau et al., 2018; Marr et al., 2018; Pontalier et al., 2018). Thus particle breakup and rearrangement instead of particle bonding is the more favored densification mode. More importantly, there is no confinement in the divergent geometry which is prerequisite for the intense plastic deformation within the bands. Moreover the rarefaction wave transmits into the particles just a few microseconds after the detonation and releases all the pressure in its wake. Thus the duration of the primary shock interaction with particle is too short to achieve high enough temperature. Therefore we are convinced that the shock consolidation is probably not the primary mechanism leading to the ensuing particle jetting. The densified aluminum fragments collected after the test is more likely to form during the interaction between the dispersed particles and the high temperature detonation gases afterwards.

The dual and single jetting mechanisms proposed in the present work are illustrated in Fig. 16. As revealed by our simulations, the primary shock only serves to compact the particle packing in a homogeneous manner (see Fig. 16(b)). The reflection of the rarefaction wave upon the outer boundary of particle shell/ring coincides with the inception of the external jetting. But the majority of particles in the wake of the rarefaction wave aren't to be pulled away immediately although the shock pressure has been released (see Fig. 16(c)). Instead the secondary shock re-compacts these stress-free particles to form an inner compact band which remains the maximum density for a relatively long time. It is the secondary shock that invokes the shear localization, which eventually results in the shear failure of the expanding particle shells/rings (see Fig. 16(d)–(g)). The secondary shock hasn't taken into account in the previous studies. The inception time of shear localization is about dozens of microseconds after the central detonation, in agreement with the emergence timescale of observed features in the particle shells (Milne et al., 2010; Milne et al., 2014; Frost et al., 2017a; Loiseau et al., 2018). Besides, the number of shear

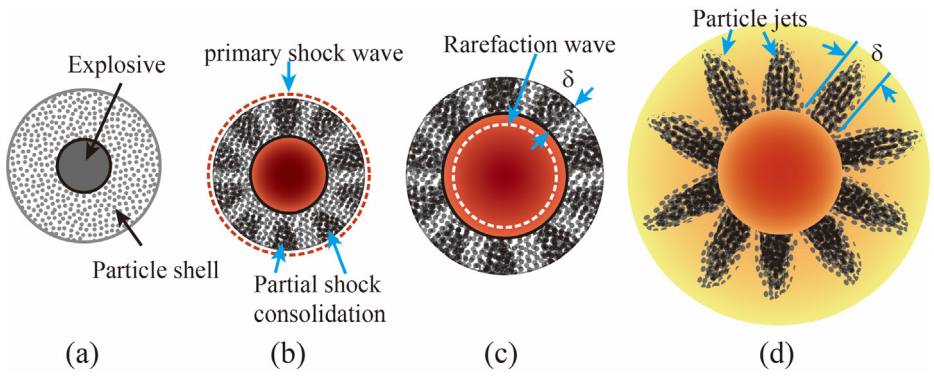

Fig. 15. Schematic of the jetting mechanism conjured in Loiseau et al. (2018) redrawn from Fig. 1 in Loiseau et al. (2018). The key event is the partial shock consolidation of particle shell during the passage of the primary shock wave (b). The reflection of the rarefaction wave causes the breakup of the partially consolidated shell with the fragments on the order of the compacted shell thickness (δ).

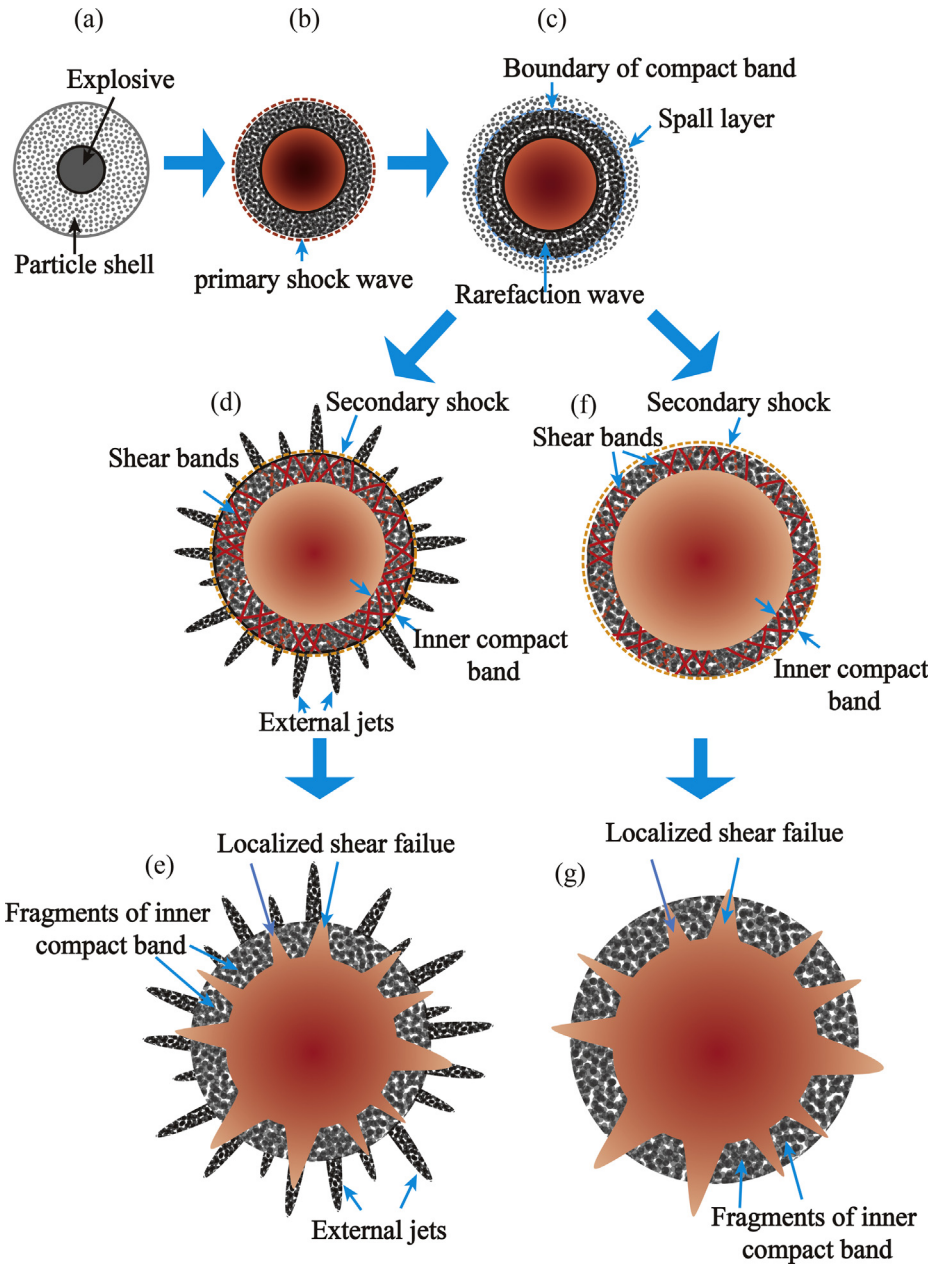

Fig. 16. Schematic of dual (a–e) and single (a–c, f, g) particle jetting mechanisms proposed in the present work.

groups in the simulated two-dimensional configuration is roughly consistent with the jet number observed in the explosive dispersal of short cylindrical particle rings (David et al., 2012).

6.2. Influences of parameters on jetting structure

The validity and applicability of the possible jetting mechanism depend on its capacity to predict the jetting structure, namely the number of jets. The jetting physics proposed in this work hasn't yet been refined enough to derive a theoretical model capable to predict the number of jets. But it suffices to identify the most determinant factors and give the qualitative correlations between the jetting structure and these factors.

The number of jets, or equivalently the average spacing between jets, is positively correlated with the average shear-band spacing, since the localized shear failure accounts for the failure of the explosive dispersed particle shells/rings. Previous studies have related the shear-band spacing in granular materials to the fragment size of the continuum media (Shih et al., 1998). Grady (2009) proposed an analytical model to predict the fragment size ($\bar{L}$), based on the assumption that the kinetic and strain energies of the material prior to fragmentation are equal to the energy required to produce the cracks. $\bar{L}$ is a function of the material resistance to crack propagation (toughness K_c), density (ρ), sonic velocity (C) and strain rate ($\dot{\varepsilon}$):

$$\bar{L} = \left(\frac{\sqrt{24}K_c}{\rho C\dot{\varepsilon}}\right)^{\frac{2}{3}} \tag{13}$$

This equation for fragment size can be extended to shear-band spacing. It incorporates the most determinant parameters, such as the strain rate ($\dot{\varepsilon}$), the packing density (ρ), as well as the resistance to shear (K_c). The granular cylinders in typical cavity inflation

experiments (Alsiny et al., 1992; MacMinn et al., 2015; Bohloli and de Pater, 2006) with the strain rate of 10^{-1}–10^{0} s^{-1} only exhibits a single or a handful of prevailing shear band opposed to the profuse shear bands observed in the explosive dispersed granular shells/rings in which the strain rate is as high as 10^{4} s^{-1} (Shih et al., 1998).

Bearing in mind that the packing density and the resistance to shear of granular materials in the scenario of our interest specifically refer to the properties of the particle packing already undergone the first divergent explosive event and the release of the ensuing rarefactions. The packing density of granular materials subjected to the secondary shock wave is approximately the maximum density of random close packing of spheres as suggested by the thick-walled cylinder experiments (Shih et al., 1998) and our simulations. Thus we argue that the shear-band spacing doesn't change much regardless of the initial packing density. But Milne et al. (2014) observed a small systematic increase in the number of primary fragments for the particle shells with lower loading packing densities. Actually the higher compressibility of the loosely packed particle shells leads to a thinner inner compact band compared with the densely packed counterparts as illustrated in Fig. 17. In both cases, the shear-band spacing is similar. But the larger perimeter of the inner surface of compact band in the initially loosely packed shell allows for the formation of more shear bands. More fragments are thus generated. Likewise using stronger explosive, the inner compact band would be thinner. Combined with increased strain rate, the particle shell dispersed by the stronger explosive is expected to break up into an increased number of finer jets, as supported by the experimental observations (Xue et al., 2014).

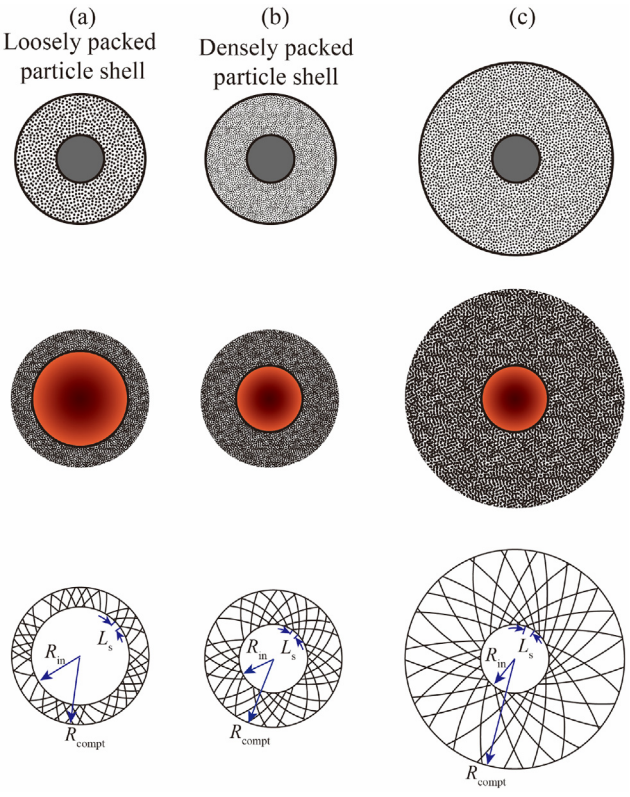

Fig. 17. Comparison of shear-banding configurations in three different particle packings. (a) Loosely packed particle shell. (b) Densely packed particle shell. (c) Particle shell with the same inner radius as in (a) and (b) but larger outer radius. The first and second columns present the initial and after-primary shock configurations of particle rings, respectively. The third column is the illustration of the shear-banding configurations in respective particle rings.

The powder fill-to-burster charge mass ratio (F/B) can be changed mainly through two ways: (1) varying the outer radius of particle shell while keeping the inner radius unchanged; (2) varying the diameter of the burster charge while the outer radius of particle shell remains constant. Surprisingly these two methods result in markedly different F/B ratio dependence of the jet number. Using the first method, Milne et al. (2014) didn't found any discernable differences in the jetting structure. Contrarily Ripley et al. (2011) reported that the number of jets increases with the decreased F/B ratio which was changed by the second way. Since the number of fragments (jets) is the function of the shear-band spacing and the inner perimeter of the inner compact band, simply changing the outer radius of particle shell within a moderate range would not have significant effects on the jet number although the strain rates slightly decreases with increased F/B ratio (see Fig. 19 (Peijun Guo and Su, 2007) (c)). By contrast, increasing the diameter of the burster charge effectively increases the inner perimeter of the inner compact band, leading to increased number of fragments (jets).

Another essential parameter defining the jetting structure is the resistance to the shear in shock compacted granular materials. Compared with the particle size, the particle morphology has more considerable effects on the shear resistance of granular materials. Flat, elongated and angular particles are found to have substantially greater shear resistance owing to both dilation and interlocking (Guo and Su, 2007; Lu et al., 2015; Guo et al., 2013). For brittle or ductile particles subjected to the explosive shock waves, they are bound to have shape significantly changed due to particle breakup (comminution) and plastic deformation (Omidvar et al., 2012; Shih et al., 1998). Therefore the brittle or ductile spherical beads, such as glass beads and aluminum powders, are to comminute or severely deform into angular or non-spherical shapes during the compaction of the primary shock, the shear resistance of the inner compact band subjected to the secondary shock being increased nontrivially. On the contrary, the hard, tough particles, such as hardened steel shot, largely retain the initial morphology even subjected to the explosive shock wave. Accordingly the inner compact band of spherical steel shots has extremely low resistance to shear flows. A much denser network of shear bands quickly extends from the inner radius to the outer boundary of band. The shear failure occurs much earlier, giving rise to a large number of much thinner jets. This deduction is substantiated by the inconspicuous particle jetting of steel shots reported by Marr et al. (2018) and Frost et al. (2017b).

6.3. Influence of the packing structure on the jetting structure

The relationship between the material fabric and the force fabric of granular materials has been extensively studied often under static-loading conditions, such as uniaxial or tri-axial loading conditions (Yang et al., 2016; Fu and Dafalias, 2011; Oda et al., 1985). Whereas very limited studies has been devoted to the correlation between the microstructures, the mesoscale deformation and the macroscale bulk responses under high strain-rate (10^{2}–10^{4} s^{-1}) loading. Specifically, Huang et al. (2016) carried out the impact compaction of SiC powders with a split Hopkinson pressure bar. The high-speed X-ray imaging and strain field mapping revealed non-uniform compaction features. Especially the compaction band is not strictly parallel to the loading direction, probably caused by heterogeneities in microstructures and stress transmission of the granular powders. The considerable softening or hardening manifested in the bulk-scale loading curves corresponds to the marked localization in compression strains.

The present work also presents a close correlation between the microstructure and the macroscale dynamic responses of particle packing specifically in a divergent cylindrical/spherical geometry.

The jetting structures emerged from the shock dispersed particle shells/rings vary substantially with the degree of the structural order. The presence of the preferential contact directions associated with the global or local structural order favors a certain form of shear-band grouping, giving rise to a distinct pattern of localized shear failure. Ultimately the resultant jetting structure changes in accordance with the microstructure.

Since the microstructure of the particle packing depends on a wide variety of parameters (Oda, 1982), including the polydispersity of particles, the particle size distribution, the particle morphology, as well as the preparation process, etc. Two particle packings consisting of identical particles but prepared differently may well possess markedly different structures, which partially accounts for the poor repeatability of the jetting experiments. On the other hand, it makes the comparison between experimental data derived from different experiments extremely challenging. Thus it is quite necessary to properly characterize the packing structure, or at least give a detailed account regarding the particle size distribution, particle morphology and the preparation method before reporting the experimental results. Numerical method has special advantages in generating particle packings with a variety of microstructures which allows us to carry out the systematic and thorough investigation into the role played by microstructure on the jetting structure.

7. Conclusion

This work presents a coupled FEM-DEM numerical framework for the direct simulation of the formation of jetting structure driven by the explosive dispersal. This framework is capable of resolving the detonation of explosive, the interaction between the detonation gases and particles, as well as the interaction between particles using realistic multibody collision model. Therefore the propagation of multiple shock waves and rarefaction wave in particles is accurately captured, which is of essence to the evolution of particle shells/rings under explosive loadings. The reflection of rarefaction wave is found to initiate the external particle jetting, while the internal particle jetting which occurs in later times arises from the localized shear failure in the inner compact band sustained by the secondary shock. This proposed jetting mechanism is consistent with the experimental observation in terms of the inception time and characteristic features of the jetting structure. The dependence of jetting structure on a variety of parameters, including the packing density, the F/B ratio, the particle size and morphology, and the material properties as well can be understood in light of the presented jetting mechanism. Furthermore the numerical studies uncover the discernable influence of the packing structure on the emergent jetting structure, which hasn't been taken into account in previous studies.

Appendix A. FEM model of explosive solids and detonation gases

Since the problems involve condensed phase explosive detonation, we use the shock-wave equation of state (EOS) for unreacted explosive and Jones-Wilkins-Lee (JWL) EOS for detonation gases. These equations are cast into the Mie-Grüneisen form by using the parameter values given in Table 3 (Price et al., 2015). The JWL EOS has parameters ω, A, B, R_1, R_2, e_0, and ρ_0 (Dobratz and Crawford, 1985). The shock-wave EOS has parameters Γ, c_0, s, α, p_0, e_0 and ρ_0. The values of these parameters can be found in literature for many explosives (Dobratz and Crawford, 1985).

Table 3
Parameters to obtain equivalent Mie- Grüneisen form.

	$\Gamma(\rho)$	$p_{\mathrm{ref}}(\rho)$	$e_{\mathrm{ref}}(\rho)$
Jones-Wilkins-Lee	ω	$Ae^{-R_1V}+Be^{-R_2V}$	$\frac{A}{\rho_0R_1}e^{-R_1V}+\frac{B}{\rho_0R_2}e^{-R_2V}-e_0$
Shock wave	$\Gamma_0(v/v_0)^{\alpha}$	$p_0+\frac{c_0^2(v_0-v)}{[v-s(v_0-v)]^2}$	$e_0+\frac{1}{2}\left[p_{ref}(\rho)+p_0\right](v_0-v)$

A programmed-burn detonation model is used to describe the conversion of the unreacted solid explosive to the reacted detonation products with the appropriate energy release. The model needs to perform threefold functions: (1) determining the ignition times t_{ig} for each computational element containing explosive; (2) calculate the reaction rate and update the reaction variable $\lambda \in [0, 1]$; 3) guarantee the energy conservation during the conversion of unreacted explosives to reacted detonation products. The ignition time for each explosive element with the Gaussian point $\mathbf{x}_c$ is

$$t_{ig}=\frac{\| \boldsymbol{x}_c-\boldsymbol{x}_d \|}{D_{CJ}}+t_0. \tag{A1}$$

The detonation starts at time t_0 from point x_d and propagates at the detonation velocity, D_{CJ}. The reaction variable in an explosive element, with an elective element size δ_{eff}, is incremented by

$$\lambda^{n+1}=\lambda^n+\Delta t\frac{D_{CJ}}{\delta_{eff}}, \tag{A2}$$

during each time step Δt, until the reaction is complete ($\lambda = 1.0$). The internal energy and pressure of the burning explosive elements are evaluated by averaging the EOS parameters (Price et al., 2015). The initial internal energy of the solid explosive includes the chemical energy of detonation, so that after the detonation is complete, the detonation products have gained the detonation energy.

The FEM module adopts an explicit forward-difference approach to simulate the detonation of explosives and the expansion of the detonation products, which comprises two main components: (1) calculate the resultant nodal forces of explosive elements, $\boldsymbol{F}_n$; (2) update the configuration of explosive elements. The resultant nodal force, $\boldsymbol{F}_n$, has three major contributions: (1) the detonation pressures when the adjoining explosive elements are ignited, $\boldsymbol{F}_d$; (2) the stresses caused by the deformation of FEM elements, $\boldsymbol{F}_e$; (3) the interaction forces arising from collision with surrounding particles, $\boldsymbol{F}_{\mathrm{p\text{-}e}}$, if there are particles in contact with the surfaces/edges having the node of interest as a vertex. The configurations of explosive elements are re-constructed every time step after updating the accelerations, $\boldsymbol{a}_{\mathrm{n}}$, velocities, $\boldsymbol{u}_{\mathrm{n}}$, and displacement, $\boldsymbol{s}_{\mathrm{n}}$, of nodes

$$\begin{cases} \boldsymbol{a}_n(t+\Delta t)=\boldsymbol{F}_n(t+\Delta t)/m_n, \\ \boldsymbol{u}_n(t+\Delta t)=\boldsymbol{u}_n(t)+\boldsymbol{a}_n(t+\Delta t)\cdot\Delta t, . \\ \boldsymbol{s}_n(t+\Delta t)=\boldsymbol{s}_n(t)+\boldsymbol{u}_n(t+\Delta t)\cdot\Delta t. \end{cases} \tag{A3}$$

where m_{n} is the effective mass of the node, Δt is the time step. The detonation pressures in each explosive element accordingly are recalculated based on the updated volumes of elements via the appropriate EOS which is a function of τ_{ig} and λ. The explicit solution scheme of the explosive domain is presented in Fig. 18.

Due to the large distortion and rotation of the explosive elements, the incremental method is adopted to calculate the deformation nodal force, $\boldsymbol{F}_e$, using the strain matrix $\mathbf{B}$ instead of the stiffness matrix of element as expressed in Eq. (A4)

$$\begin{cases} \Delta\boldsymbol{\varepsilon}_i=\boldsymbol{B}_i\Delta\boldsymbol{u}_e \\ \Delta\boldsymbol{\sigma}_i=\boldsymbol{D}\Delta\boldsymbol{\varepsilon}_i \\ \boldsymbol{\sigma}_i(t+\Delta t)=\boldsymbol{\sigma}(t)+\Delta\boldsymbol{\sigma}_i \\ \boldsymbol{F}_e=\sum_{i=1}^{N}\boldsymbol{B}_i^T\boldsymbol{\sigma}_i(t+\Delta t)w_iJ_i \end{cases}, \tag{A4}$$

where $\mathbf{B}_i$, $\Delta\varepsilon_i$, $\Delta\sigma_i$, w_i, J_i are the strain matrix, incremental strain, incremental stress, integral coefficient, and Jacobi determinant in Gaussian point i; $\mathbf{D}$, $\Delta\mathbf{u}_e$ are the elastic matrix and incremental displacement vector of element, respectively; N is the total number

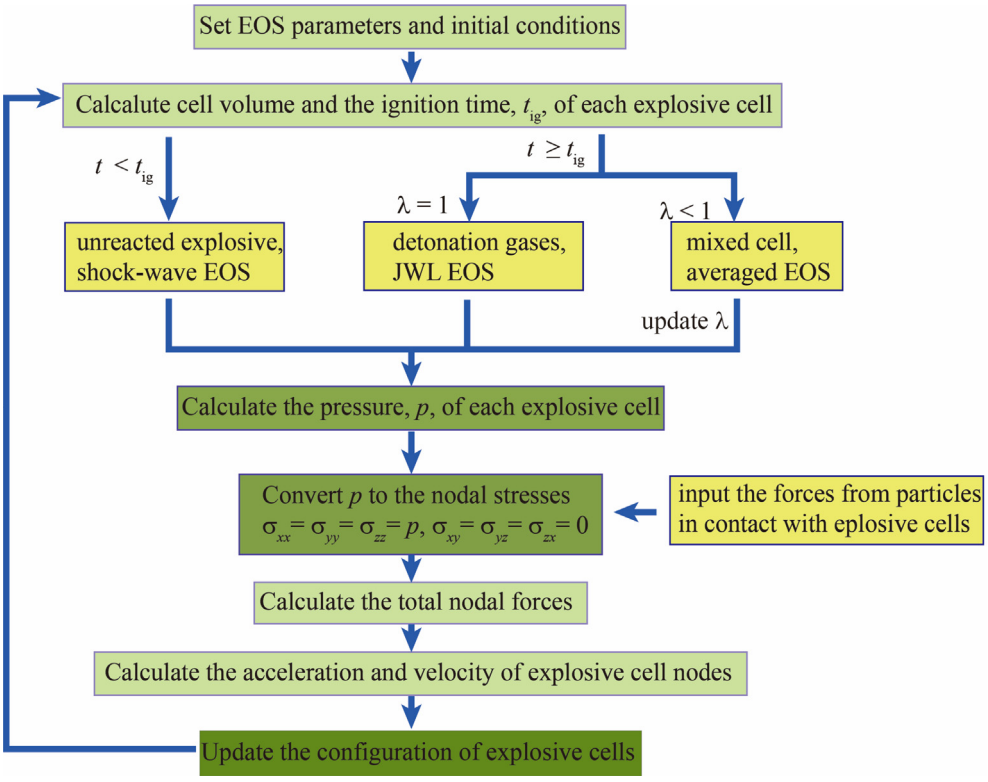

Fig. 18. Solution scheme of the explosive FEM module.

of Gaussian points. Note that $\mathbf{B}_i$ should be renewed at each time step.

If node **O** has $n_{element}$ adjoining elements and surfaces/edges with node **O** as one vertex are in contact with n_{partice} particles, the total forces exerted on node **O**, $\boldsymbol{F}_n^{\boldsymbol{O}}$ is given by

$$\begin{aligned}\boldsymbol{F}_n^{\boldsymbol{O}} &= \boldsymbol{F}_d^{\boldsymbol{O}} + \boldsymbol{F}_e^{\boldsymbol{O}} + \boldsymbol{F}_{p-e}^{\boldsymbol{O}} + \boldsymbol{F}_{damp}^{\boldsymbol{O}} \\ &= \sum_{k=1}^{n_{cell}} \boldsymbol{F}_{d,k}^{\boldsymbol{O}} + \sum_{k=1}^{n_{cell}} \boldsymbol{F}_{e,k}^{\boldsymbol{O}} + \sum_{l=1}^{n_{particle}} \boldsymbol{F}_{p-e,l}^{\boldsymbol{O}} - \alpha \left| \boldsymbol{F}_d^{\boldsymbol{O}} + \boldsymbol{F}_{p-e}^{\boldsymbol{O}} \right| \frac{\dot{\boldsymbol{u}}^{\boldsymbol{O}}}{\left| \dot{\boldsymbol{u}}^{\boldsymbol{O}} \right|}, \end{aligned} \tag{A5}$$

where $\boldsymbol{F}_{d,k}^{\boldsymbol{O}}$ and $\boldsymbol{F}_{e,k}^{\boldsymbol{O}}$ represent the detonation pressure and deformation force from the adjoining explosive element k, respectively; $\boldsymbol{F}_{p-e,l}^{\boldsymbol{O}}$ represents collision force exerted on a node **O** by the particle l; $\boldsymbol{F}_{damp}^{\boldsymbol{O}}$ is a global non-viscous damping force used to absorb part of kinetic energy of node **O**. α is the global damping ratio.

Fig. 19(a) shows the schematic of meshes at the outer edge of the explosive which is confined by particle layers. Six explosive elements denoted by *i*-*n* have a common vertex, **O**. Thus the detonation pressure and deformation forces of node **O** have contributions from these six neighboring elements. These elements are either unreacted explosive, or detonation gases, or the mixture of solids and gases. Since there are no edges with node **O** as one vertex in contact with particles, $\boldsymbol{F}_{p-e}^{\boldsymbol{O}} = 0$ in this case. But for node **A**, two edges **AB** and **AC** are in contact with particles (see Fig. 19 (b)). Thus the collision forces between particles and explosive elements should be taken into account for node **A**. The coupling procedure between FEM and DEM will be presented in Appendix C.

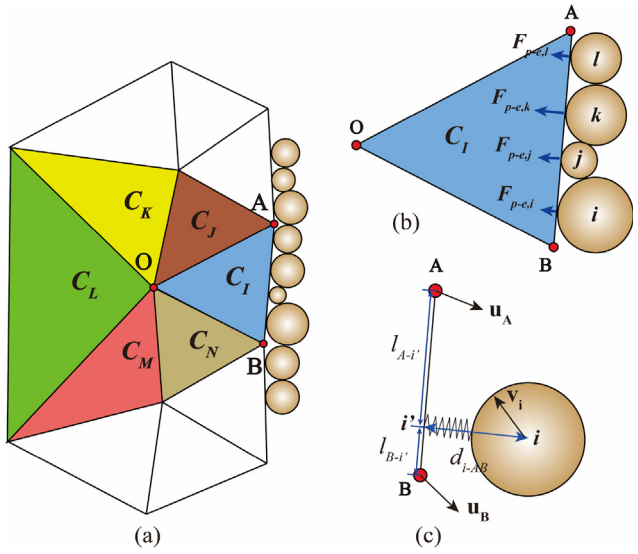

Fig. 19. (a) Schematic of the arrangement of the explosive elements (triangular elements) and the particles surrounding the edges of the explosive FEM domains; (b) Zoomed-in schematic of the explosive element in contact with particles; (c) Schematic showing the interaction between the edge of explosive element and the particle in contact.

Appendix B. DEM model of particles

The DEM proposed by Cundall and Strack in 1980s is a first-principle approach to simulation granular materials (Cundall and Strack, 1979). It takes into account the interactions between particles and between particles and surrounding media. The trajectory of each particle is tracked by solving Newton's second law of motion.

$$\begin{aligned} m_i \frac{d\boldsymbol{v}_i}{dt} &= \sum_j \boldsymbol{F}_{ij} + \boldsymbol{F}_{i,e-p} + m_i \boldsymbol{g} \\ I_i \frac{d\omega_i}{dt} &= \sum_j \boldsymbol{M}_{ij} + \boldsymbol{M}_{i,e-p} \end{aligned} \tag{B1}$$

where m_i, I_i are the mass and rotational inertia of particle i, $\boldsymbol{v}_i$ and ω_i are the translational and rotational velocities, $\boldsymbol{g}$ is the gravity acceleration, $\boldsymbol{F}_{ij}$ and $\boldsymbol{M}_{ij}$ denote the force and torque on particle i resulting from neighboring particle j, $\boldsymbol{F}_{i,e\text{-}p}$ and $\boldsymbol{M}_{i,e\text{-}p}$ represent the force and torque on particle i resulting from the explosive element in contact with particle i. Thus no assumptions on the constitutive relationship of granular materials are needed in this approach. A good review of its theoretical background and major applications has been presented by Zhu et al. (2007). Recently a comprehensive review of the extension of DEM to the non-spherical particle systems is given by Lu et al. (2015).

In our simulations, the contact force between particles is described by a spring-dashpot model in the normal direction, and a spring-slider model along the tangential direction. The normal and tangential forces between the particle pair i and j, F_n^{ij} and F_t^{ij} are calculated in an incremental manner

$$\begin{aligned} F_n^{ij}(t+\Delta t) &= F_n^{ij}(t) + K_n \Delta\delta_n^{ij} - F_{n,damp}^{ij} \\ &= F_n^{ij}(t) + K_n\left[(\boldsymbol{v}_i - \boldsymbol{v}_j)\Delta t\right]\cdot \boldsymbol{n}_{ij} - 2\xi\sqrt{K_n m_{eff}}(\boldsymbol{v}_i - \boldsymbol{v}_j)\cdot \boldsymbol{n}_{ij} \\ F_t^{ij}(t+\Delta t) &= \begin{cases} \text{if } F_t^{ij}(t+\Delta t) < \mu\left|F_n^{ij}(t+\Delta t)\right| \\ F_t^{ij}(t) + K_t\Delta\delta_t^{ij} = F_t^{ij}(t) + K_t\left[(\boldsymbol{v}_i - \boldsymbol{v}_j)\Delta t\right]\cdot \boldsymbol{s}_{ij} \\ \text{else} \\ \mu\left|F_n^{ij}(t+\Delta t)\right| \end{cases}, \end{aligned} \tag{B2}$$

where $\Delta\delta_n^{ij}$and $\Delta\delta_t^{ij}$ are the increments of the normal and tangential overlaps, respectively; K_n and K_t are the effective normal and tangential stiffness, respectively; ξ is the critical damping ratio; μ is the friction coefficient between particles. K_n and K_t are the function of effective Young's and shear moduli, Y_{eff} and G_{eff}.

$$\begin{cases} K_n = Y_{eff}, K_t = G_{eff} \text{ for 2D} \\ K_n = \pi R_{eff} Y_{eff}, K_t = \pi R_{eff} G_{eff} \text{ for 3D} \end{cases}, \quad Y_{eff} = \frac{Y_i + Y_j}{2}, G_{eff} = \frac{G_i + G_j}{2}, \frac{1}{R_{eff}} = \frac{1}{R_i} + \frac{1}{R_j}, \frac{1}{m_{eff}} = \frac{1}{m_i} + \frac{1}{m_j} \tag{B3}$$

where Y_i (Y_j) and G_i (G_j) are the Young's and shear moduli of particle i (j), respectively; R_i and R_j are the radii of particle i and j, respectively. ξ is given as a function related to the restitution coefficient, ε,

$$\xi = \frac{\ln\varepsilon}{\sqrt{\ln^2(\varepsilon) + \pi^2}} \tag{B4}$$

Appendix C. Interaction between the FEM elements and discrete elements

The coupling algorithm of the FEM and the DEM incorporates three sequent steps: (1) contact detention; (2) calculation of interaction forces between particles and the FEM elements in contact; (3) interpolating the interaction forces into FEM nodes. The most time-consuming step in the coupling algorithm of FEM and DEM is contact detection, which is normally divided into two substeps: coarse contact detection and fine contact detection (Feng et al., 2014). In coarse contact detection, the particles in the neighborhood of a specified elemental surface/edge are detected and recorded because only the neighboring particles have a chance of making contact with the surface/edge of interest. Subsequently the fine contact detection step is invoked to determine which particle(s) actually is (are) in contact with the surface/edge of interest. Two criteria should be satisfied when the particle-surface/edge contact is established: (1) the distance between the mass center of the particle and the surface/edge should be equal to or less than the particle radius; (2) the projection of the mass center of the particle should be within the surface/edge. Specifically, tor the two-dimensional configuration as illustrated in Fig. 19(c), these two criteria require

$$\begin{cases} d_{i-AB} \leqslant R_i \\ l_{A-i'} \leqslant l_{AB},\ l_{B-i'} \leqslant l_{AB} \end{cases} \tag{C1}$$

where $d_{i\text{-}AB}$ is the distance between particle i and the FEM elemental edge **AB**, $l_{A-i'}$ and $l_{B-i'}$ are the distances of the edge vertices **A** and **B** to the projection of the mass center of particle i, l_{AB} is the length of edge.

The interaction force between the particle and elemental surface/edge in contact is aligned with the normal direction of the surface/edge. Thus only normal interaction force is activated

$$\boldsymbol{F}_{p-e}(t+\Delta t) = \boldsymbol{F}_{p-e}(t) + K_n^{p-e}[(\boldsymbol{v}_i - \boldsymbol{u}_{i'})\Delta t]\cdot \boldsymbol{n} \tag{C2}$$

where K_n^{p-e} represents contact stiffness between particle and FEM elemental surface/edge, $\boldsymbol{u}_{i'}$ is the velocity vector of the projection point of the mass center of particle, a weighted average over those of nodes **A** and **B**,

$$\boldsymbol{u}_{i'} = \chi_A \boldsymbol{u}_A + (1-\chi_A)\boldsymbol{u}_B = \frac{l_{A-i'}}{l_{AB}}\boldsymbol{u}_A + \frac{l_{B-i'}}{l_{AB}}\boldsymbol{u}_B. \tag{C3}$$

In order to ensure the detonation pressure exert on surrounding particles at the instants the detonation front reaches the edges of explosive, K_n^{p-e} is set to several orders larger than the contact stiffness between particles.

Since the contact point between particle and FEM elemental surface/edge normally is not right on the nodes of FEM meshes, $\boldsymbol{F}_{\mathbf{p\text{-}e}}$ would be re-distributed to the nodes using the linear shape function as used in Eq. (C3).

The time increment for DEM model depends on the smallest mass and the elastic modulus of particles, while the time increment for FEM model depends on the characteristic length of FEM elements which changes as the explosive domain rapidly expands. The coupling algorithm chooses the smaller time increment to ensure the numerical stability.

References

Alsiny, A., Vardoulakis, I., Drescher, A., 1992. Deformation localization in cavity inflation experiments on dry sand. Geotechnique 42, 395–410.

Bai, C.-H., Wang, Y., Xue, K., Wang, L.-F., 2018. Experimental study of detonation of large-scale powder–droplet–vapor mixtures. Shock Waves 28, 599–611.

Balakrishnan, K., 2014. Explosion-driven Rayleigh-Taylor instability in gas-particle mixtures. Phys. Fluids 26, 043303.

Bohloli, B., de Pater, C.J., 2006. Experimental study on hydraulic fracturing of soft rocks: Influence of fluid rheology and confining stress. J. Petrol. Sci. Eng. 53, 1–12.

Borg, J.P., Vogler, T.J., Fraser, A., 2009. A review of mesoscale simulations of granular materials. AIP Conf. Proc. 1195, 1331–1336.

Cundall, P.A., Strack, O.D.L., 1979. A discrete numerical model for granular assemblies. Geotechnique 29, 47–65.

David, L.F., Yann, G., Oren, P., Samuel, G., Fan, Z., 2012. Particle jet formation during explosive dispersal of solid particles. Phys. Fluids 24, 091109.

Desmond, K.W., Weeks, E.R., 2014. Influence of particle size distribution on random close packing of spheres. Phys. Rev. E 90, 022204.

Dobratz, B., Crawford, P., 1985. LLNL Explosives Handbook: Properties of Chemical Explosives and Explosive Stimulants. Lawrence Livermore National Laboratory, Springfield, VA.

Feng, C., Li, S., Liu, X., Zhang, Y., 2014. A semi-spring and semi-edge combined contact model in CDEM and its application to analysis of Jiweishan landslide. J. Rock Mech. Geotech. Eng. 6, 26–35.

Frost, D.L., Gregoire, Y., Goroshin, S., Zhang, F., 2011. Interfacial instabilities in explosive gas-particle flows. 23rd International Colloquium on the Dynamics of Explosions and Reactive Systems. University of California, Irvine, USA.

Frost, D.L., Loiseau, J., Goroshin, S., Zhang, F., Milne, A., Longbottom, A., 2017a. Fracture of explosively compacted aluminum particles in a cylinder. AIP Conf. Proc. 1793, 120019.

Frost, D.L., Loiseau, J., Marr, B.J., Goroshin, S., 2017b. Particle segregation during explosive dispersal of binary particle mixtures. AIP Conf. Proc. 1793, 120020.

Frost, D.L., 2018. Heterogeneous/particle-laden blast waves. Shock Waves 28, 439–449.

Fu, P., Dafalias, Y.F., 2011. Fabric evolution within shear bands of granular materials and its relation to critical state theory. Int. J. Numer. Anal. Meth. Geomech. 35, 1918–1948.

Grégoire, Y., David, F., Oren, P., 2011. Development of instabilities in explosively dispersed particles. AIP Conf. Proc. 1426, 1623–1626.
Grady, D.E., 2009. Dynamic Fragmentation of Solids, Shock Wave Science and Technology Reference Library. Springer, Berlin Heidelberg, pp. 1–108.
Guo, P., Su, X., 2007. Shear strength, interparticle locking, and dilatancy of granular materials. Can. Geotech. J. 44, 579–591.
Guo, Y., Wassgren, C., Hancock, B., Ketterhagen, W., Curtis, J., 2013. Granular shear flows of flat disks and elongated rods without and with friction. Phys. Fluids 25, 063304.
Hanifpour, M., Francois, N., Robins, V., Kingston, A., Vaez Allaei, S.M., Saadatfar, M., 2015. Structural and mechanical features of the order-disorder transition in experimental hard-sphere packings. Phys. Rev. E 91, 062202.
Huang, J.Y., Lu, L., Fan, D., Sun, T., Fezzaa, K., Xu, S.L., Zhu, M.H., Luo, S.N., 2016. Heterogeneity in deformation of granular ceramics under dynamic loading. Scr. Mater. 111, 114–118.
Huang, Y.J., Chan, C.K., Zamankhan, P., 2010. Granular jet impingement on a fixed target. Phys. Rev. E 82, 031307.
Kieffer, S.W., 1981. Blast dynamics at Mount St Helens on 18 May 1980. Nature 291, 568.
Loiseau, J., Pontalier, Q., Milne, A.M., Goroshin, S., Frost, D.L., 2018. Terminal velocity of liquids and granular materials dispersed by a high explosive. Shock Waves 28, 473–487.
Lu, G., Third, J.R., Müller, C.R., 2015. Discrete element models for non-spherical particle systems: From theoretical developments to applications. Chem. Eng. Sci. 127, 425–465.
MacMinn, C.W., Dufresne, E.R., Wettlaufer, J.S., 2015. Fluid-driven deformation of a soft granular material. Phys. Rev. X 5, 011020.
Marr, B.J., Pontalier, Q., Loiseau, J., Goroshin, S., Frost, D.L., 2018. Suppression of jet formation during explosive dispersal of concentric particle layers. AIP Conf. Proc. 1979, 110011.
Milne, A., Parrish, C., Worland, I., 2010. Dynamic fragmentation of blast mitigants. Shock Waves 20, 41–51.
Milne, A.M., Floyd, E., Longbottom, A.W., Taylor, P., 2014. Dynamic fragmentation of powders in spherical geometry. Shock Waves 24, 501–513.
Milne, A.M., 2016. Gurney analysis of porous shells. Propellants Explos. Pyrotech. 41, 665–671.
Mo, H., Lien, F.-S., Zhang, F., Cronin, D.S., 2018. A numerical framework for the direct simulation of dense particulate flow under explosive dispersal. Shock Waves 28, 559–577.
Oda, M., 1982. Fabric tensor for discontinuous geological materials. Soils Found. 22, 96–108.
Oda, M., Nemat-Nasser, S., Konishi, J., 1985. Stress-induced anisotropy in granular masses. Soils Found. 25, 85–97.
Omidvar, M., Iskander, M., Bless, S., 2012. Stress-strain behavior of sand at high strain rates. Int. J. Impact Eng. 49, 192–213.
Osnes, A.N., Vartdal, M., Pettersson Reif, B.A., 2018. Numerical simulation of particle jet formation induced by shock wave acceleration in a Hele-Shaw cell. Shock Waves 28, 451–461.
Ouellet, F., Annamalai, S., Rollin, B., 2017. Effect of a bimodal initial particle volume fraction perturbation in an explosive dispersal of particles. AIP Conf. Proc. 1793, 150011.
Pontalier, Q., Loiseau, J., Goroshin, S., Frost, D.L., 2018. Experimental investigation of blast mitigation and particle–blast interaction during the explosive dispersal of particles and liquids. Shock Waves 28, 489–511.
Price, M.A., Nguyen, V.-T., Hassan, O., Morgan, K., 2015. A method for compressible multimaterial flows with condensed phase explosive detonation and airblast on unstructured grids. Comput. Fluids 111, 76–90.
Rigby, S.E., Fay, S.D., Tyas, A., Clarke, S.D., Reay, J.J., Warren, J.A., Gant, M., Elgy, I., 2018. Influence of particle size distribution on the blast pressure profile from explosives buried in saturated soils. Shock Waves 28, 613–626.
Ripley, R., Donahue, L., Zhang, F., 2011. Jetting instabilities of particles from explosive dispersal. AIP Conf. Proc. 1426, 1615–1618.
Ripley, R.C., Zhang, F., 2014. Jetting instability mechanisms of particles from explosive dispersal. J. Phys.: Conf. Ser. 500, 152012.
Ritzel, D.V., Ripley, R.C., Murray, S.B., Anderson, J., 2009. Near-field Blast Phenomenology of Thermobaric Explosions. Springer Berlin Heidelberg, Berlin, Heidelberg, pp. 305–310.
Schreck, C.F., O'Hern, C.S., Silbert, L.E., 2011. Tuning jammed frictionless disk packings from isostatic to hyperstatic. Phys. Rev. E 84, 011305.
Shi, Z.-H., Li, W.-F., Qian, W.-W., Liu, H.-F., Wang, F.-C., 2017. Liquid-like granular film from granular jet impact. Chem. Eng. Sci. 162, 1–9.
Shih, C.J., Meyers, M.A., Nesterenko, V.F., 1998. High-strain-rate deformation of granular silicon carbide. Acta Mater. 46, 4037–4065.
Steinhardt, P.J., Nelson, D.R., Ronchetti, M., 1983. Bond-orientational order in liquids and glasses. Phys. Rev. B 28, 784–805.
Sun, J.I.N., Sundaresan, S., 2011. A constitutive model with microstructure evolution for flow of rate-independent granular materials. J. Fluid Mech. 682, 590–616.
Vidyapati, V., Subramaniam, S., 2016. A constitutive model for dense granular flows based on microstructural descriptors. Ind. Eng. Chem. Res. 55, 10178–10190.
Vogler, T.J., Lee, M.Y., Grady, D.E., 2007. Static and dynamic compaction of ceramic powders. Int. J. Solids Struct. 44, 636–658.
Wang, L., Li, S., Zhang, G., Ma, Z., Zhang, L., 2013. A GPU-based parallel procedure for nonlinear analysis of complex structures using a coupled FEM/DEM approach. Math. Problems Eng. 2013, 15.
Xu, N., Blawzdziewicz, J., O'Hern, C.S., 2005. Random close packing revisited: Ways to pack frictionless disks. Phys. Rev. E 71, 061306.
Xu, T., Lien, F.-S., Ji, H., Zhang, F., 2013. Formation of particle jetting in a cylindrical shock tube. Shock Waves 23, 619–634.
Xue, K., Li, F., Bai, C., 2013. Explosively driven fragmentation of granular materials. Eur. Phys. J. E 36, 1–16.
Xue, K., Yu, Q., Bai, C., 2014. Dual fragmentation modes of the explosively dispersed granular materials. Eur. Phys. J. E 37, 88.
Yang, L.-T., Li, X., Yu, H.-S., Wanatowski, D., 2016. A laboratory study of anisotropic geomaterials incorporating recent micromechanical understanding. Acta Geotech. 11, 1111–1129.
Yongbo, F., Shihai, L., Yang, Z., Zhiyong, F., Xiaoyu, L., 2016. Lessons learned from the landslides in Shengli east open-pit mine and north open-pit mine in Xilinhot City, Inner Mongolia Province, China. Geotech. Geol. Eng. 34, 425–435.
Yuan, R., Shen, B., 2017. Numerical modelling of the contact condition of a Brazilian disk test and its influence on the tensile strength of rock. Int. J. Rock Mech. Min. Sci. 93, 54–65.
Zheng, Q.J., Xu, M.H., Chu, K.W., Pan, R.H., Yu, A.B., 2017. A coupled FEM/DEM model for pipe conveyor systems: Analysis of the contact forces on belt. Powder Technol. 314, 480–489.
Zhu, H.P., Zhou, Z.Y., Yang, R.Y., Yu, A.B., 2007. Discrete particle simulation of particulate systems: theoretical developments. Chem. Eng. Sci. 62, 3378–3396.